Bull. Mater. Sci. (2022) 45:34
https://doi.org/10.1007/s12034-021-02610-3

Investigation of structural, mechanical and optoelectronic properties of cubic $Cd_{1-x-y}Zn_xHg_ySe$ quaternary alloys through first-principle calculations

SAYANTIKA CHANDA, MANISH DEBBARMA, DEBANKITA GHOSH, BIMAL DEBNATH and SURYA CHATTOPADHYAYA*
Department of Physics, Tripura University, Suryamaninagar 799022, India
*Author for correspondence (surya_ju@yahoo.com)

MS received 27 July 2021; accepted 7 October 2021

Abstract. Structural, mechanical and optoelectronic features of zinc-blende $Cd_{1-x-y}Zn_xHg_ySe$ quaternary alloys as well as allied binary compounds and ternary alloys have been investigated through first-principle calculations. Computed elastic stiffness constants ensure that each specimen is mechanically stable, ductile, elastically anisotropic and compressible. The covalent bonding plays a superior role over ionic bonding in each specimen. The phonon dispersion spectra ensure that each binary compound is dynamically stable, while each ternary or quaternary alloy exhibits dynamical instability. Each semiconductor alloy exhibits a direct (Γ–Γ) bandgap. Electrons possess lower effective mass compared to holes. Electrons excited from the Se-4p state of valence band to Zn-5s, Cd-6s and Hg-7s states of conduction band contribute peaks in dielectric function spectra of the considered specimens. Computed oscillator strength of quaternary alloys reveals availability of adequate number of electrons in respective conduction bands. On the basis of computed optoelectronic properties, the alloys would be suitable to fabricate near-UV and UV optoelectronic devices.

Keywords. $Cd_{1-x-y}Zn_xHg_ySe$; first-principle calculations; structural and mechanical properties; mBJ-GGA and PBE+U; optoelectronic properties.

1. Introduction

Tuning of physical properties of some elemental or compound semiconductors through formation of alloys is necessary in materials engineering to get the desired properties for fabricating a specific device. Formation of quaternary alloys of a set of more than two compounds is treated as advanced procedure in such tuning process compared to that of ternary alloys, where properties of only a couple of compounds can be tuned. In the last couple of decades, $A_xB_yC_{1-x-y}D$ quaternary alloys have been extensively designed for diverse target-oriented applications. They are enclosed with three systems A_xB_yC, $A_xC_{1-x}D$ and $B_yC_{1-y}D$ of ternary alloys and synthesized with three binary compounds AD, BD and CD, which should be selected appropriately to achieve the desired goal.

The binary compounds under group IIB-VIA, the zinc-blende (B3) diatomic cadmium, zinc and mercury selenides CdSe, ZnSe and HgSe are treated as very important optoelectronic materials [1]. Experiments on CdSe and ZnSe reveal that they possesses wide and direct-bandgap (Γ–Γ) semiconductor properties. In contrast, different experiments have suggested that HgSe possess zero-gap [2], negative bandgap [3] and marginally positive fundamental bandgap [4]. Their mixed ternary and quaternary alloys, thin films and miscellaneous nanostructures have diversified photovoltaic, optoelectronic, spintronic and luminescence applications [5–14].

In the past several decades, diverse properties of CdSe, ZnSe and HgSe have been investigated experimentally [15–26]. Such properties were also studied theoretically through several first-principle calculations [27–45]. In addition, thin films of CdZnSe ternary alloys [46], $Zn_{1-x}Cd_xSe$/ZnSe heterostructures [47], quantum dots [48,49], ZnCdSe/ZnSe single-quantum wells [50], $Zn_{1-x}Cd_xSe$/MgSe multiple quantum wells [51], etc. were prepared and their optoelectronic properties were characterized experimentally. Gas source molecular beam epitaxial growth of wide-bandgap $Zn_{1-x}Hg_xSe$ alloys [52] was investigated. Band structure of $Hg_{1-x}Cd_xSe$ mixed crystals was also investigated from the inter-band magneto-absorption experiment [53].

Supplementary Information: The online version contains supplementary material at https://doi.org/10.1007/s12034-021-02610-3.

On the theoretical side, several significant calculations on Cd and Zn chalcogenides based on diverse clusters, monolayers and quantum-dots have been performed so far [54–59]. Density-functional calculations of structural and electronic properties of stoichiometric zinc-blende, wurtzite and rocksalt CdSe clusters as well as nonstoichiometric zinc-blende CdSe clusters [54] and later the structural, electronic and optical properties of ligand-free Zn_mSe_n clusters [55] were performed. The effect of surface passivation on structural, electronic and optical properties of stoichiometric Zn_nSe_n clusters were studied theoretically [56]. Self-consistent charge density-functional tight-binding method was applied to explore tight-binding parameters for Zn-X (X = Zn, O, S, Se, Te, Cd, H, C and N) for large-scale quantum-mechanical simulation of various zinc-chalcogenides nanostructures [57]. Using quantum confinement, controlling of biexciton recombination in quasi-type-I and II CdSe/CdS core/shell spherical quantum dots were studied theoretically [58]. First-principle calculations were also carried out to investigate stability and electronic structure of two-dimensional CP3 monolayer to find the area of their potential applications [59]. Moreover, optoelectronic features of bulk CdZnSe [60], HgCdSe [61] and HgZnSe [62,63] ternary specimens were also investigated from first-principle calculations.

It is to be noted that none of the experimental or theoretical investigation is carried out on any of the said features of $Cd_{1-x-y}Zn_xHg_ySe$ quaternary alloys to search their probable applications. Therefore, experimental or theoretical studies on structural, elastic and optoelectronic characteristics of cubic $Cd_{1-x-y}Zn_xHg_ySe$ quaternary specimens would show a new horizon in their diversified mechanical and optoelectronic applications. Motivated by these facts, we have carried out the present calculations, which is the introductory initiative for exploring the said characteristics of zinc-blende $Cd_{1-x-y}Zn_xHg_ySe$ quaternary specimens. The same for the allied zinc-blende binary CdSe, ZnSe and HgSe as well as CdZnSe, HgCdSe and HgZnSe ternary specimens are also calculated. Change in structural, mechanical, electronic and optical features in $Cd_{1-x-y}Zn_xHg_ySe$ triangular quaternary system within Zn concentration (x) at each considered Hg concentration (y) and vice versa are computed elaborately.

2. Method of calculations

All-electron density functional theory (DFT) [64,65] based FP-LAPW [66] calculations is carried out with the WIEN2K code [67]. The Phonopy code [68] is employed to investigate dynamical stability/instability of the cubic crystals with computation of respective phonon dispersion spectra. The cubic-elastic code [69] is employed to calculate elastic properties of the cubic crystals.

The PBE-GGA [70] is applied in structural and elastic properties, while mBJ-GGA [71] and PBE+U [72,73] methods are applied in electronic and optical properties to compute exchange-correlation (XC) potentials. Electronic features with PBE-GGA are modified with Coulomb repulsion between valence d-electrons of transition elements through Hubbard parameter U [74] in the PBE+U approach. At U = 10.0, 8.0 and 6.0 eV, calculated bandgap of ZnSe, CdSe, and HgSe and their respective experimentally measured data are observed to be closest to each other during the variation of respective calculated bandgaps with U. We have selected them as U for 3d, 4d and 5d electrons of zinc, cadmium and mercury atoms, respectively, in case of calculations of electronic and optical features with PBE+U.

On the basis of the muffin-tin (MT) model, the FP-LAPW approach considers that atoms exist inside the MT spheres. The wavefunction in this region is expanded with spherical harmonics by selecting $l_{\max} = 10$ as the largest angular momentum. Considering largest cut-off wave vector $K_{\max} = 8.0/R_{MT}$ and magnitude of largest vector $G_{\underline{\max}} = 16\ \mathrm{Ry}^{1/2}$ in the Fourier expansion of the charge density, the plane wave basis is used to expand the wavefunction in the interstitial region. The selected MT-sphere radius holding cadmium, zinc, mercury and selenium atoms as 2.4, 2.3, 2.5 and 2.3 a.u., respectively, ensures non-overlapping atomic spheres as well as preventing any charge leakage from the respective core. The optimum k-mesh is selected as 10 × 10 × 10 by varying total energy as a function of the number of k-points. The core states are separated from valence states with a core-cut-off energy –6.0 Ry. The fully relativistic approximation for core, but scalar relativistic approximation for valence electrons is employed. Total energy convergence is acquired through self-consistent-field approximation. In such an approximation, the total energy difference 10^{-5} Ry between two consecutive steps is selected to be the threshold for the termination of iterations.

The designing processes of diverse unit cells of the specimens under the $Cd_{1-x-y}Zn_xHg_ySe$ system have been described in the Section-I of the supplementary materials. For visualization of designed crystal structures, the graphic code XCrySDen [75] is used. Optimized zinc-blende crystal structures of $Cd_{0.50}Zn_{0.25}Hg_{0.25}Se$, $Cd_{0.25}Zn_{0.25}Hg_{0.50}Se$ and $Cd_{0.25}Zn_{0.50}Hg_{0.25}Se$ quaternary alloys are presented as supplementary figure S1a–c, respectively, in the supplementary materials.

3. Results and discussions

3.1 *Structural properties*

3.1a *Lattice constant and bulk modulus a_0* and *B_0*: The optimized lattice constant (a_0) and bulk modulus (B_0) for each designed unit cell are evaluated from fitting of self-consistently computed respective energy–volume curve to Murnagran's equation of state [76]. Computed a_0 and B_0 are presented in table 1. In the case of diatomic specimens, excellent closeness between computed a_0 and B_0 and respective experimental data are observed [1,17]. They also agree fairly well with a few respective earlier theoretically calculated data [27–30,35,39,62]. Structural data for any type of alloy does not exist in the literature.

3.1b *Concentration dependence of lattice constant and bulk modulus*: Figure 1a displays the variations of computed a_0 as function of Hg-concentration (y) at each Zn-concentration (x) and vice-versa, while figure 1b displays the same of computed B_0 in the $\mathrm{Cd}_{1-x-y}\mathrm{Zn}_x\mathrm{Hg}_y\mathrm{Se}$ triangular quaternary system. Here, a_0 increases almost linearly in figure 1a, while B_0 decreases nonlinearly in figure 1b with increasing y at any particular x. We have observed a completely reverse picture with increasing x at any particular y. Repeated replacement of cadmium atom(s) of lower diameter (0.322 nm) with mercury atom(s) of relatively bigger diameter (0.342 nm) causes the increase in a_0 in the former. In contrast, successive replacement of cadmium atom(s) of bigger diameter (0.322 nm) with zinc atom(s) of relatively smaller diameter (0.284 nm) reduces a_0 in the latter.

Figure 1c shows decrease in a_0 with increasing x in the $\mathrm{Zn}_x\mathrm{Cd}_{1-x}\mathrm{Se}$ system and with increasing x or reducing y (= 1–x) in the $\mathrm{Zn}_x\mathrm{Hg}_y\mathrm{Se}/\mathrm{Zn}_x\mathrm{Hg}_{1-x}\mathrm{Se}$ system due to

Table 1. Calculated a_0, B_0 (with energy–volume curve), C_{11}, C_{12}, C_{44}, C', G_V, G_R and G_H for all the specimens.

x	y	Specimen	a_0 (Å)	B_0 (GPa) (from E–V curve)	C_{11} (GPa)	C_{12} (GPa)	C_{44} (GPa)	C' (GPa)	G_V (GPa)	G_R (GPa)	G_H (GPa)
0.0	0.0	CdSe	6.198	56.52	77.85	47.41	32.68	15.22	25.70	22.40	24.05
			6.05[a*]	53.0[a*]	88.1[c]	53.6[c]	27.4[c]				13.6[h*]
			6.035[a]	66.5[a]	55.4[d]	37.7[d]	18.9[d]				13.3[e]
			6.025[b]	65.12[c]	58.8[e]	48.9[e]	25.2[e]				11.3[f]
			6.05[c]	45.16[d]	81.2[f]	47.8[f]	22.9[f]				13.6[p]
			6.216[d]		86.2[g]	30.3[g]	36.8[g]				
	0.25	$\mathrm{Cd}_{0.75}\mathrm{Hg}_{0.25}\mathrm{Se}$	6.211	55.44	75.74	46.64	30.61	14.55	24.19	21.23	22.71
	0.50	$\mathrm{Cd}_{0.50}\mathrm{Hg}_{0.50}\mathrm{Se}$	6.227	54.15	73.47	45.83	28.51	13.82	22.63	20.01	21.32
	0.75	$\mathrm{Cd}_{0.25}\mathrm{Hg}_{0.75}\mathrm{Se}$	6.245	52.67	71.29	45.06	26.21	13.12	20.97	18.73	19.85
	1.0	HgSe	6.263	51.35	69.14	44.27	23.92	12.43	19.33	17.47	18.40
			6.074[a*]	57.6[a*]	60.8[c*]	44.6[c*]	22.3[c*]		23.2[k]	13.8[k]	23.1[j]
			6.194[a]	41.8[a]	61.0[d*]	44.0[d*]	22.0[d*]				18.5[k]
			6.14[h]	56.36[h]	69.00[e*]	51.05[e*]	23.07[e*]				15.4[p]
			6.11[i]	53.9[i]	62.2[f*]	46.4[f*]	22.7[f*]				
					74.5[j],	50.7[j]	44.1[j]				
					52.69[k]	37.99[k]	33.69[k]				
					50.7[l]	43.7[l]	30.3[l]				
0.25	0.0	$\mathrm{Cd}_{0.75}\mathrm{Zn}_{0.25}\mathrm{Se}$	6.105	59.30	79.70	48.27	34.63	15.72	27.06	23.38	25.22
	0.25	$\mathrm{Cd}_{0.50}\mathrm{Zn}_{0.25}\mathrm{Hg}_{0.25}\mathrm{Se}$	6.119	56.40	77.59	47.50	32.56	15.04	25.55	22.21	23.88
	0.50	$\mathrm{Cd}_{0.25}\mathrm{Zn}_{0.25}\mathrm{Hg}_{0.50}\mathrm{Se}$	6.140	55.19	75.32	46.69	30.46	14.32	24.00	20.99	22.50
	0.75	$\mathrm{Zn}_{0.25}\mathrm{Hg}_{0.75}\mathrm{Se}$	6.161	55.59	73.14	45.92	28.16	13.61	22.34	19.72	21.03
0.50	0.0	$\mathrm{Cd}_{0.50}\mathrm{Zn}_{0.50}\mathrm{Se}$	5.998	61.73	81.55	49.13	36.58	16.21	28.43	24.34	26.39
	0.25	$\mathrm{Cd}_{0.25}\mathrm{Zn}_{0.50}\mathrm{Hg}_{0.25}\mathrm{Se}$	6.019	60.65	79.44	48.36	34.51	15.54	26.92	23.19	25.06
	0.50	$\mathrm{Zn}_{0.50}\mathrm{Hg}_{0.50}\mathrm{Se}$	6.040	59.53	77.17	47.55	32.41	14.81	25.37	21.97	23.67
0.75	0.0	$\mathrm{Cd}_{0.25}\mathrm{Zn}_{0.75}\,\mathrm{Se}$	5.878	64.01	83.40	49.99	38.53	16.71	29.80	25.31	27.55
	0.25	$\mathrm{Zn}_{0.75}\mathrm{Hg}_{0.25}\mathrm{Se}$	5.902	63.01	81.29	49.22	36.46	16.03	28.29	24.15	26.22
1.0	0.0	ZnSe	5.738	66.34	85.25	50.85	40.48	17.20	31.17	26.26	28.72
			5.67[a*]	62.5[a*]	85.9[b*]	50.6[b*]	40.6[b*]				
			5.667[b*]	64.7[b*]	81.0[g*]	48.8[g*]	44.1[g*]				
			5.591[a]	83.3[a]	94.0[m]	61.0[m]	64.0[m]				
			5.588[b]	75.68[h]	95.9[n]	53.6[n]	48.9[n]				
			5.65[h]	71.82[m]	82.45[o]	42.71[o]	35.5[o]				
			5.624[m]								

Experimental data: [a*][1], [b*][17], [c*][16], [d*][15], [e*][18], [f*][19], [g*][20], [h*][21].
Previous theoretical data: [a][27], [b][28], [c][29], [d][30], [e][31], [f][32], [g][33], [h][62], [i][35], [j][36], [k][37], [l][38], [m][39], [n][40], [o][41], [p][34].

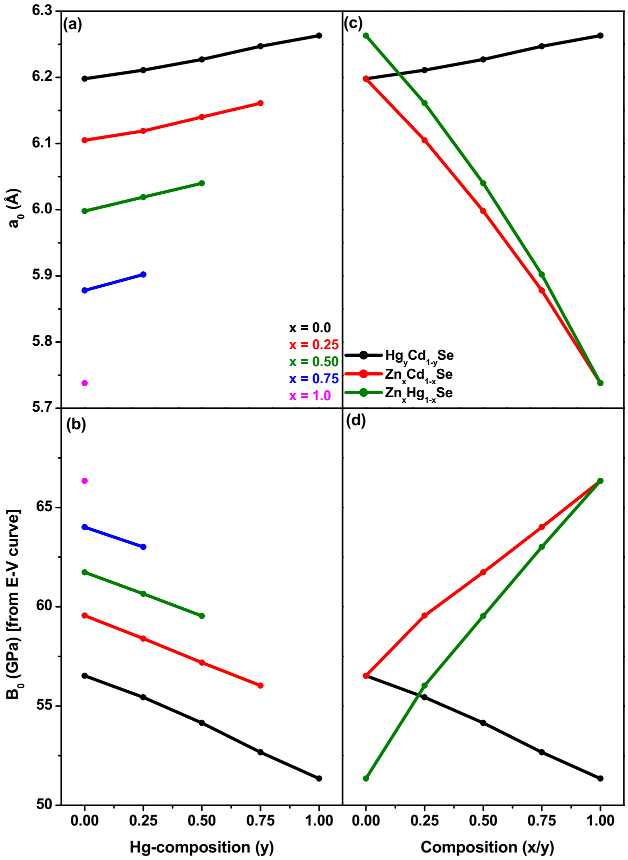

Figure 1. (**a**) Hg-composition (y) dependence curves of computed a_0 for the compounds under $Cd_{1-x-y}Zn_xHg_ySe$ quaternary system. (**b**) Hg-composition (y) dependence curves of computed B_0 for the compounds under $Cd_{1-x-y}Zn_xHg_ySe$ quaternary system. (**c**) Composition (x/y) dependence curves of computed a_0 for the ternary alloys. (**d**) Composition (x/y) dependence curves of computed B_0 for the ternary alloys.

replacement of larger cadmium and mercury, respectively, with smaller zinc atom(s). Also, a_0 enhances with increasing y in the $Hg_yCd_{1-y}Se$ system due to the replacement of smaller cadmium with larger mercury atom(s). The compositional variation of a_0 is opposite to that of B_0 in any of the aforesaid variations in figure 1d because change in B_0 is inversely proportional to that of equilibrium volume $V_0 = a_0^3$ of any cubic cell.

Figure 1c and d shows slight deviation of composition dependence curves of a_0 and B_0, respectively, from the corresponding linear dependence curve [77] for the $Zn_xCd_{1-x}Se$, $Hg_yCd_{1-y}Se$ and $Zn_xHg_{1-x}Se$ systems. The following quadratic equations represent such marginal nonlinearity in $a_0(x)$ or $a_0(y)$ curve for each ternary system

$$a_0^{\mathrm{ZnCdSe}}(x) = xa_0^{\mathrm{ZnSe}} + (1-x)a_0^{\mathrm{CdSe}} - x(1-x)b^a_{\mathrm{ZnCdSe}} \tag{1}$$

$$a_0^{\mathrm{HgCdSe}}(x) = xa_0^{\mathrm{HgSe}} + (1-x)a_0^{\mathrm{CdSe}} - x(1-x)b^a_{\mathrm{HgCdSe}} \tag{2}$$

$$a_0^{\mathrm{ZnHgSe}}(x) = xa_0^{\mathrm{ZnSe}} + (1-x)a_0^{\mathrm{HgSe}} - x(1-x)b^a_{\mathrm{ZnHgSe}} \tag{3}$$

Here, lattice constant of ZnSe, CdSe and HgSe is a_0^{ZnSe}, a_0^{CdSe} and a_0^{HgSe}, respectively. Also, b^a_{ZnCdSe}, b^a_{HgCdSe} and b^a_{ZnHgSe} is the bowing parameter in composition dependence curve of lattice constant for the $Zn_xCd_{1-x}Se$, $Hg_yCd_{1-y}Se$ and $Zn_xHg_{1-x}Se$ ternary system, respectively. Similar quadratic equations also represent the marginal nonlinearities in $B_0(x)$ or $B_0(y)$ curves for the three ternary systems. In this case, b^B_{ZnCdSe}, b^B_{HgCdSe} and b^B_{ZnHgSe} are treated as bowing parameter in the composition dependence curve of bulk modulus for $Zn_xCd_{1-x}Se$, $Hg_yCd_{1-y}Se$ and $Zn_xHg_{1-x}Se$ ternary system, respectively.

The a_0 *vs.* composition (x or y) curve for $Zn_xCd_{1-x}Se$ and $Zn_xHg_{1-x}Se$ systems show marginally upward deviation, while $Hg_yCd_{1-y}Se$ system shows marginally downward deviation from respective linear variation as per Vegard's law [77]. In contrast, the compositional (x or y) variation of the B_0 curve in case of each of the $Zn_xCd_{1-x}Se$, $Zn_xHg_{1-x}Se$ and $Hg_yCd_{1-y}Se$ systems shows very small upward deviation from the corresponding linear variation. From quadratic fit of each of the $a_0(x)$ or $a_0(y)$ curve, calculated lattice constant bowing parameter is found as $b^a_{\mathrm{ZnCdSe}} = -0.1223$ Å, $b^a_{\mathrm{ZnHgSe}} = -0.1611$ Å and $b^a_{\mathrm{HgCdSe}} = 0.0137$ Å for the $Zn_xCd_{1-x}Se$, $Zn_xHg_{1-x}Se$ and $Hg_yCd_{1-y}Se$ system, respectively. From the quadratic fit of the $B_0(x)$ or $B_0(y)$ curve, the calculated bulk modulus bowing parameter is $b^B_{\mathrm{ZnCdSe}} = -1.206$ GPa, $b^B_{\mathrm{HgCdSe}} = -2.618$ GPa and $b^B_{\mathrm{ZnHgSe}} = -0.7669$ GPa for the $Zn_xCd_{1-x}Se$, $Zn_xHg_{1-x}Se$ and $Hg_yCd_{1-y}Se$ system, respectively.

3.2 *Thermodynamic and dynamical stability/instability*

3.2a *Thermodynamic stability/instability*: Thermodynamic stability/instability of a crystalline alloy can be investigated through calculation of its formation energy. The energy of formation of $A_xB_{1-x}C$ (i.e., $Zn_xCd_{1-x}Se$, $Zn_xHg_{1-x}Se$ and $Hg_yCd_{1-y}Se$) ternary alloys and for $Cd_{1-x-y}Zn_xHg_ySe$ (i.e., $A_{1-x-y}B_xC_yD$) quaternary alloys are calculated by the relations, given below

$$E^{\mathrm{form}}_{\mathrm{Ternary}}(x) = E_0^{A_xB_{1-x}C} - xE_0^{AC} - (1-x)E_0^{BC} \tag{4}$$

$$E^{\mathrm{form}}_{\mathrm{Quaternary}}(x,y) = E_0^{A_{1-x-y}B_xC_yD} - xE_0^{BD} - yE_0^{CD} - (1-x-y)E_0^{AD} \tag{5}$$

Clearly, $E_0^{A_xB_{1-x}C}$ indicates total energy of any of the said ternary alloys in equation (4), while $E_0^{A_{1-x-y}B_xC_yD}$ is the total energy of the $Cd_{1-x-y}Zn_xHg_ySe$ quaternary specimens at any composition pair (0.25, 0.25), (0.25, 0.50) and (0.50, 0.25) in equation (5). The E_0^{AC}, E_0^{BC}, E_0^{BD}, E_0^{CD} and E_0^{AD} are the total energy of any of the diatomic ZnSe, HgSe and CdSe, involved in each ternary or quaternary system. Computed formation energy *vs.* compositions (x, y) contour plots for all the alloys of the $Cd_{1-x-y}Zn_xHg_ySe$ system are presented in figure 2. The formation of any thermodynamically stable ternary alloy at each x or $y = 0.25, 0.50, 0.75$ as well as quaternary alloy at (0.25, 0.25), (0.25, 0.50) and (0.50, 0.25) composition pair is ensured with negative value of formation energy, calculated using equations (4) and (5), respectively.

3.2b *Dynamical stability/instability*: The dynamical stability or instability of any specimen allied to the $Cd_{1-x-y}Zn_xHg_ySe$ system is investigated by calculating respective phonon dispersion spectra. The computed phonon dispersion spectra for CdSe, ZnSe and HgSe in the W-L-Γ-X-W-K direction of high symmetry are presented in figure 3a–c, respectively. The same for $Cd_{0.50}Zn_{0.25}Hg_{0.25}Se$, $Cd_{0.25}Zn_{0.25}Hg_{0.50}Se$ and $Cd_{0.25}Zn_{0.50}Hg_{0.25}Se$ quaternary alloys along the R-Γ-X-M-Γ direction are presented in figure 4a–c, respectively. For x or y = 0.25, 0.50 and 0.75, the calculated phonon dispersion spectra for the ternary alloys under the $Zn_xCd_{1-x}Se$, $Hg_yCd_{1-y}Se$ and $Zn_xHg_{1-x}Se$ systems are presented as supplementary figures S2a–c, S3a–c and S4a–c, respectively.

Clearly, the dynamical stability of zinc-blende CdSe, ZnSe and HgSe under the ambient conditions are confirmed because no imaginary/negative frequency is present in the respective phonon dispersion spectra. In contrast, the presence of negative frequencies in the phonon dispersion spectra of each ternary or quaternary alloy under the same conditions is the signature of respective dynamical instability.

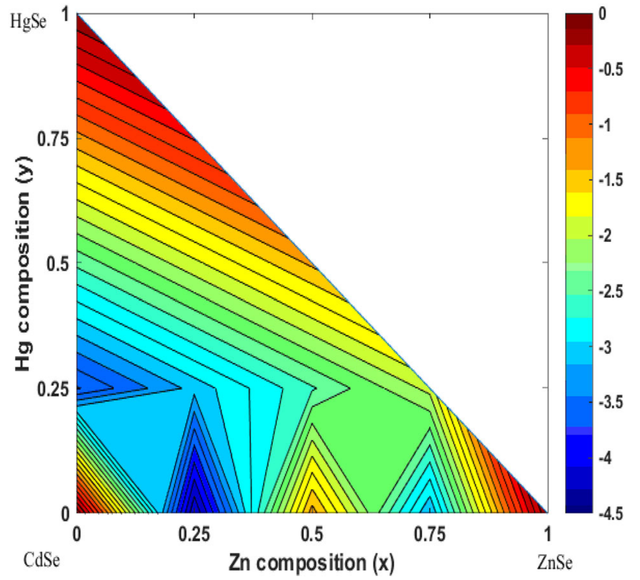

Figure 2. Computed formation energy *vs.* compositions contour plot for the ternary and quaternary alloys under the $Cd_{1-x-y}Zn_xHg_ySe$ system.

3.3 *Elastic properties*

3.3a *Elastic stiffness constants* (C_{ij}) *of cubic specimens*: Generally, 36 independent elastic stiffness constants are associated with any crystal. But the lattice symmetry due to identical axes in a cubic crystal reduces the number to three only. The C_{11} is associated with elasticity along the length, while both the C_{12} and C_{44} are associated with the elasticity related to the shape of a cubic lattice.

In tables 1–3, calculated elastic stiffness constants (C_{11}, C_{12} and C_{44}) and related mechanical features of all the cubic specimens are available. Tables 1–3 also contain experimentally measured and previously calculated data of some of the parameters of binary compounds for comparison, while any such data for ternary and quaternary alloys do not exist in the literature. For each specimen, the observed trend is $C_{11} > C_{12} > C_{44}$ in table 1, but it could be validated only with experimental data for HgSe [15,16,18,19] and ZnSe [17,20] as well as previous calculated data for CdSe [29–31]. Each specimen satisfies Born's mechanical stability criteria for a cubic crystal [69] and hence exhibits mechanical stability. Inequality in C_{44} and calculated shear constant $C' = (C_{11}–C_{12})/2$ with $C_{44} > C'$ in table 1 has established elastic anisotropy of each cubic crystal [69]. Calculated constants C_{11}, C_{12} and C_{44} reduce, in figure 5a–c, respectively, in the $Cd_{1-x-y}Zn_xHg_ySe$ system with increasing mercury concentration (y) at each selected zinc concentration (x). Conversely, any of them enhances with increasing zinc concentration (x) at each selected mercury concentration (y). In the case of HgSe and ZnSe, computed C_{11}, C_{12} and C_{44} and the corresponding experimentally observed data are extremely close to each other [15–20]. The same for CdSe shows proximity to some corresponding earlier calculated data [29–33].

3.3b *Elastic moduli, constants and isotropy/anisotropy*: Directly or indirectly in terms of C_{11}, C_{12} and C_{44}, we have computed shear modulus (G) proposed by Voigt (G_V), Reuss (G_R) and Hill (G_H) along with bulk modulus (B_0) and Young's modulus (Y) of each cubic crystal. Larger value of each of them of a material is a signature of its superior rigidity and vice versa [69]. Calculated diverse shear modulus for all the considered specimens are also included in table 1, but B_0 and Y are included in table 2. In the case of our considered specimens, the minimum stiffness is shown by HgSe and maximum by ZnSe. Again, $C_{11} > B_0 > C_{12}$ for each specimen in tables 1 and 2 is indicating respective mechanical stability [69]. Computed B_0 of each specimen from the energy–volume curve and that with corresponding

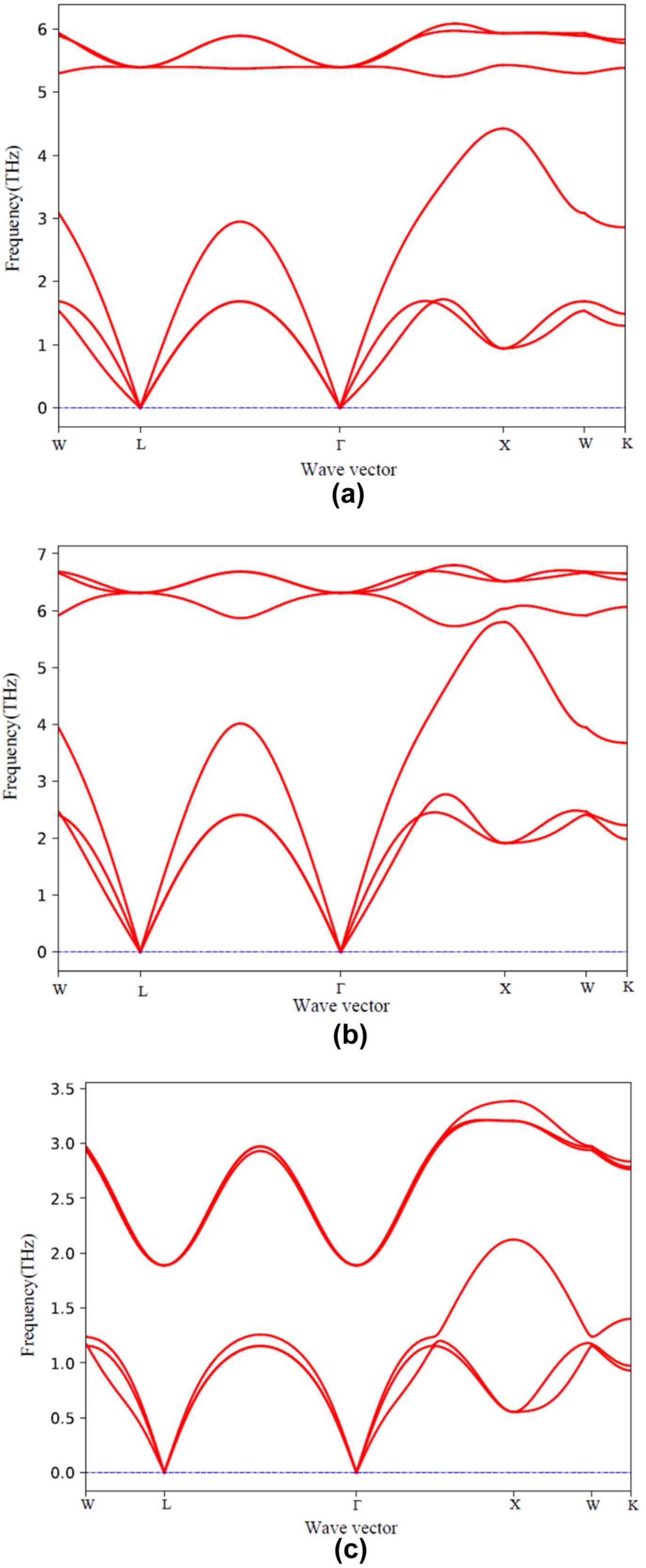

Figure 3. Computed phonon dispersion spectra of zinc-blende binary: (**a**) CdSe, (**b**) ZnSe and (**c**) HgSe.

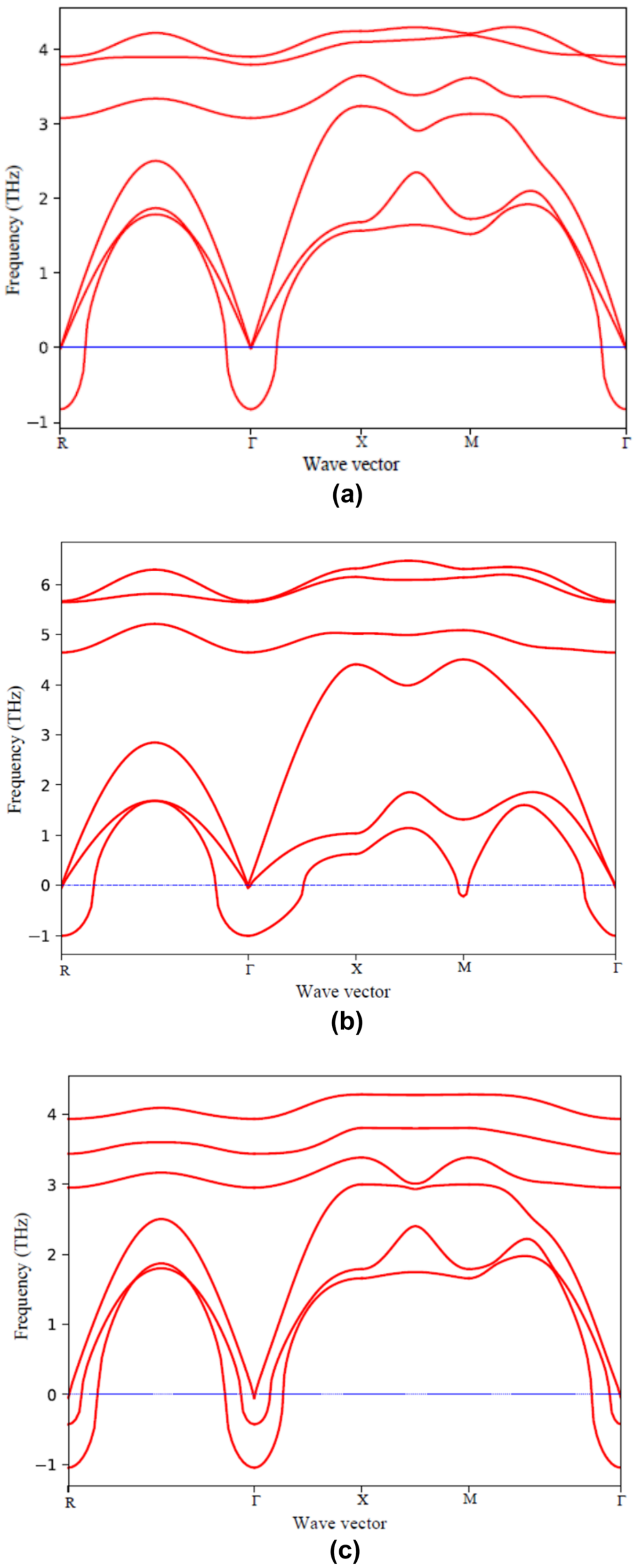

Figure 4. Computed phonon dispersion spectra of zinc-blende: (**a**) $Cd_{0.50}Zn_{0.25}Hg_{0.25}Se$, (**b**) $Cd_{0.25}Zn_{0.25}Hg_{0.50}Se$ and (**c**) $Cd_{0.25}Zn_{0.50}Hg_{0.25}Se$ quaternary alloy.

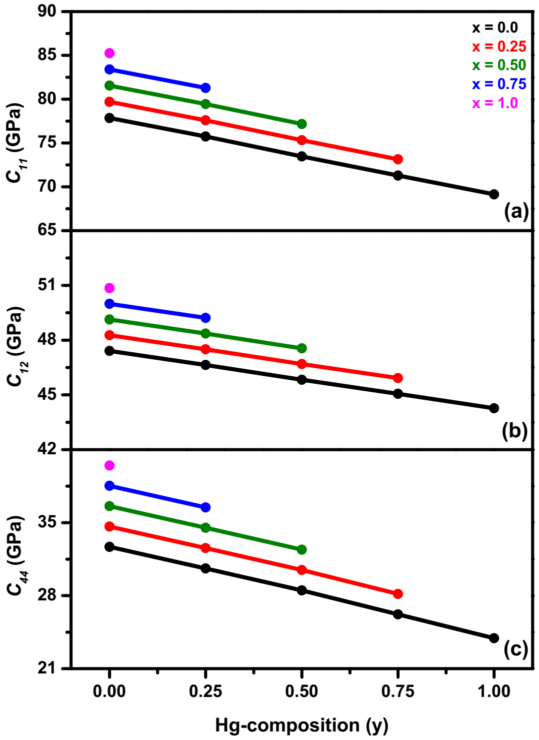

Figure 5. Hg-composition (y) dependence curve of computed (**a**) C_{11}, (**b**) C_{12}, (**c**) C_{44} for the compounds under $Cd_{1-x-y}Zn_x Hg_y Se$ quaternary system.

C_{11} and C_{12} are nearly equal. Any of the calculated G_V, G_R, G_H, B_0 and Y in the $Cd_{1-x-y}Zn_xHg_ySe$ system reduces, as shown in supplementary figure S5a–c, respectively, with growing mercury concentration (y) at each selected zinc concentration (x). Conversely, each of them enhances with growing zinc concentration (x) at each selected mercury concentration (y).

The ratio B_0/C_{44} calculates the plastic behaviour [78], while both Cauchy's pressure ($C^{//} = C_{12}–C_{44}$) and Pugh's ratio (B_0/G_H) calculate the ductile or brittle behaviour of a material [79]. The calculated B_0/C_{44}, B_0/G_H and $C^{//}$ for each specimen are presented in table 2. The $B_0/C_{44} > 1.5$ indicate that all the specimens are plastic. The computed $B_0/G_H > 2.1$ and the positive sign of $C^{//}$ indicate their ductility [69]. In supplementary figure S6, the correlation between $C^{//}$ and B_0/G_H again confirms ductility of all the specimens.

The Poisson's ratio (σ) is calculated with G_H and B_0 of a material [69]. For a cubic specimen, Kleinman parameter (ξ) of a cubic crystal is evaluated by C_{11} and C_{12} [69]. In table 2, calculated σ in the range 0.300–0.343 ensures that each specimen is highly compressible, ductile, plastic and contains a central type of inter-atomic bonding force [69]. The calculated ξ in the range 0.704–0.739 ensure that bending plays major role over stretching in chemical bonds in all the specimens [69]. In

Table 2. Calculated B_0 (by C_{11} and C_{12}), Y, B_0/C_{44}, B_0/G_H, σ, ξ, $C^{//}$, A_Z and C_{11}/C_{12} for all the specimens.

x	y	Specimen	B_0 (GPa) (by C_{11} and C_{12})	Y (GPa)	B_0/C_{44}	B_0/G_H	σ	ξ	$C^{//}$ (GPa)	A_Z	C_{11}/C_{12}
0.0	0.0	CdSe	57.56	63.33 36.8^a, 61.20^b 45.8^c	1.761	2.393 3.92^a	0.317 0.383^a 0.345^b	0.715 0.883^a	14.73	2.147 5.091^a 1.59^b	1.642
	0.25	$Cd_{0.75}Hg_{0.25}Se$	56.34	60.06	1.840	2.481	0.322	0.720	16.03	2.104	1.624
	0.50	$Cd_{0.50}Hg_{0.50}Se$	55.04	56.65	1.931	2.582	0.328	0.726	17.32	2.062	1.603
	0.75	$Cd_{0.25}Hg_{0.75}Se$	53.80	53.03	2.053	2.710	0.336	0.733	18.85	1.998	1.582
	1.0	HgSe	52.56	49.42 61.8^d, 48.52^e	2.197	2.857 $>1.75^d$ 2.32^e	0.343 0.337^d 0.311^e	0.739	20.35	1.924 5.25^d	1.562 1.35^{a*}
0.25	0.0	$Cd_{0.75}Zn_{0.25}Se$	58.75	66.19	1.696	2.329	0.312	0.712	13.64	2.204	1.651
	0.25	$Cd_{0.50}Zn_{0.25}Hg_{0.25}Se$	57.53	62.94	1.767	2.409	0.318	0.717	14.94	2.164	1.633
	0.50	$Cd_{0.25}Zn_{0.25}Hg_{0.50}Se$	56.23	59.55	1.846	2.500	0.324	0.723	16.23	2.127	1.613
	0.75	$Zn_{0.25}Hg_{0.75}Se$	54.99	55.96	1.953	2.615	0.330	0.730	17.76	2.069	1.593
0.50	0.0	$Cd_{0.50}Zn_{0.50}Se$	59.94	69.03	1.639	2.271	0.308	0.709	12.55	2.257	1.660
	0.25	$Cd_{0.25}Zn_{0.50}Hg_{0.25}Se$	58.72	65.81	1.701	2.344	0.313	0.714	13.85	2.221	1.643
	0.50	$Zn_{0.50}Hg_{0.50}Se$	57.42	62.43	1.772	2.426	0.319	0.720	15.14	2.188	1.623
0.75	0.0	$Cd_{0.25}Zn_{0.75}$ Se	61.13	71.86	1.586	2.219	0.304	0.707	11.46	2.307	1.668
	0.25	$Zn_{0.75}Hg_{0.25}Se$	59.91	68.65	1.643	2.285	0.309	0.712	12.76	2.274	1.652
1.0	0.0	ZnSe	62.32	74.68	1.539	2.170	0.300	0.704	10.37	2.354	1.676

Experimental data: [a*][18].
Previous theoretical data: [a][31], [b][29], [c][32], [d][36], [e][37].

terms of C_{11}, C_{12} and C_{44}, computed Zener anisotropy factor (A_Z) with $A_Z \neq 1$ stands for a varying mode of anisotropy, while $A_Z = 1$ stands for total isotropy of a crystal [69]. The computed $A_Z > 1.9$ for all the considered specimens in table 2 is a clear indication of elastically anisotropic nature with the largest inflexibility along the <111> diagonal of the cubic crystal [69].

3.3c *Bonding characteristics*: The C_{11}/C_{12} having values 1.0, 2.0, and in between them indicate totally ionic, totally covalent and a mixture of covalent and ionic bonding, respectively, in a zinc-blende crystal [80]. Computed C_{11}/C_{12} in between 1.562 and 1.676, presented in table 2, is indicating mixture of covalent and ionic bonding with the supremacy of the former in any specimen. The Phillips ionicity (f_i) for all the zinc-blende crystals is calculated in terms of respective C_{11} and C_{12} [79] and presented in table 3. They are found in the range 0.632–0.685. For CdSe, HgSe and ZnSe, computed f_i is extremely close to the corresponding experimentally measured f_i for CdSe [22], HgSe [23] and ZnSe [22].

3.3d *Acoustic phonon velocities and thermal properties*: In a crystal, velocities of longitudinal (v_l) and transverse (v_t) acoustic phonon waves are calculated with G_H and B_0 of the crystal, while that for mean acoustic phonon wave (v_m) is calculated with v_l and v_t [79]. The Debye temperature (Θ_D) differentiates the quantum and classical characteristics of phonons in a solid. Since acoustic phonon vibrations result in their vibrational excitations at low temperatures, the Θ_D is computed in terms of v_m at $T<\Theta_D$ [79]. In the thermal transport phenomenon, the Debye frequency (ω_D) of a solid is the uppermost boundary of frequency of phonon vibration and it is calculated as a function of Θ_D [81]. The minimum thermal conductivity of a material (K_{min}) is calculated with mean acoustic phonon wave velocity (v_m) using an empirical relationship [82]. Another empirical formula has been suggested to calculate the melting temperature (T_m) of a cubic material in terms of its C_{11} [83]. Table 3 includes computed v_l, v_t, v_m, Θ_D, ω_D, K_{min} and T_m for all the considered specimens. The computed v_l and v_t for HgSe show fair closeness to the respective earlier calculated data [37,42]. The calculated Θ_D for HgSe shows fair closeness to the corresponding experimental data [16]. Table 3 again indicates that calculated K_{min} for HgSe exists within the experimentally investigated range [16]. The computed T_m for HgSe exhibits fair closeness to the corresponding experimentally investigated data [16]. In the $Cd_{1-x-y}Zn_xHg_ySe$ system, supplementary figure S7a–d, displays reduction in computed Θ_D, ω_D, K_{min} and T_m, respectively, with growing Hg concentration (y) at any particular Zn concentration (x). In contrast, each of them shows enhancement with growing Zn concentration (x) at any particular Hg concentration (y).

In most of the cases, we have observed that if a crystal system shows dynamical stability, it also shows mechanical stability. If a crystal system exhibits both mechanical and

Table 3. Calculated f_i, v_t, v_l, v_m, Θ_D, ω_D, K_{min} and T_m for all the specimens.

x	y	Specimen	f_i	v_t (m s^{-1})	v_l (m s^{-1})	v_m (m s^{-1})	Θ_D (K)	ω_D (THz)	K_{min} (W m^{-1}.K^{-1})	T_m (K)
0.0	0.0	CdSe	0.647 0.699[a*]	2123	4098	2376	362.4 167[c]	7.551	0.861	1013
	0.25	$Cd_{0.75}Hg_{0.25}Se$	0.656	1959	3827	2195	334.1	6.961	0.792	1001
	0.50	$Cd_{0.50}Hg_{0.50}Se$	0.665	1814	3590	2034	308.8	6.435	0.730	987
	0.75	$Cd_{0.25}Hg_{0.75}Se$	0.675	1682	3383	1888	285.7	5.952	0.673	974
	1.0	HgSe	0.685 0.68[b*] 0.62[a] 0.76[b]	1560 1569[d] 1635[e]	3194 2998[d]	1753	264.5 151[c*] 242[d*] 231[b] 264.30[d]	5.512	0.622 0.1–3.5[d*]	962 1072[d*]
0.25	0.0	$Cd_{0.75}Zn_{0.25}Se$	0.643	2193	4198	2454	380.0	7.917	0.916	1024
	0.25	$Cd_{0.50}Zn_{0.25}Hg_{0.25}Se$	0.651	2021	3910	2263	349.6	7.285	0.841	1012
	0.50	$Cd_{0.25}Zn_{0.25}Hg_{0.50}Se$	0.661	1872	3665	2098	323.0	6.729	0.774	998
	0.75	$Zn_{0.25}Hg_{0.75}Se$	0.670	1736	3449	1947	298.7	6.224	0.714	985
0.50	0.0	$Cd_{0.50}Zn_{0.50}Se$	0.639	2260	4291	2527	398.3	8.299	0.977	1035
	0.25	$Cd_{0.25}Zn_{0.50}Hg_{0.25}Se$	0.647	2081	3991	2329	365.8	7.621	0.894	1022
	0.50	$Zn_{0.50}Hg_{0.50}Se$	0.656	1925	3732	2155	337.4	7.029	0.822	1009
0.75	0.0	$Cd_{0.25}Zn_{0.75}Se$	0.636	2323	4379	2596	417.6	8.701	1.046	1046
	0.25	$Zn_{0.75}Hg_{0.25}Se$	0.643	2135	4060	2387	382.4	7.967	0.954	1033
1.0	0.0	ZnSe	0.632 0.676[a*]	2379	4453	2657	437.8	9.122	1.123	1057

Experimental data: [a*][22], [b*][23], [c*][18], [d*][16].
Previous theoretical data: [a][36], [b][38], [c][31], [d][37], [e][42].

dynamical stability in a particular crystallographic phase, then it is the stable phase of that crystal. But in a particular phase, if a crystal system shows both mechanical and dynamical instability then it is the unstable phase of that crystal and those systems are insignificant to study.

On the other hand, if a crystal system is mechanically stable but dynamically unstable and vice-versa in a particular phase, then it can be treated as a possible meta-stable phase of the crystal. In our case, all the ternary and quaternary specimens investigated are mechanically stable but dynamically unstable so that zinc-blende is their meta-stable phase.

Dynamical instability takes place at a non-zero critical frequency and involves all the mechanical problems in which the time is included. In the equilibrium state, this is subjected to a dynamic loading on structural–mechanical systems either by sudden shock and impact loading or hydro-elastic forces or pulsating parametric forces. In this case, the sudden instabilities of periodic motions can occur when a structural system is loaded by periodic excitation, such as vibration of atoms in crystals, etc. So, it is basically a highly multidisciplinary problem, which has an immense impact on diverse fields of materials science and structural engineering. Therefore, though our ternary alloys are dynamically unstable but mechanically stable, we have studied the electronic and optical properties of these meta-stable zinc-blende ternary and quaternary alloys.

3.4 *Electronic properties*

3.4a *Band structure and bandgap*: In case of the quaternary system $Cd_{1-x-y}Zn_xHg_ySe$, though mBJ-GGA caters band structure profile of any alloy with direct bandgap (Γ–Γ) qualitatively similar to those with PBE+U scheme, the former provides larger bandgap compared to the latter. Since atomic orbitals of all the constituent atoms contribute to the band structure of only the $Cd_{0.50}Zn_{0.25}Hg_{0.25}Se$, $Cd_{0.25}Zn_{0.25}Hg_{0.50}Se$ and $Cd_{0.25}Zn_{0.50}Hg_{0.25}Se$ quaternary alloys, their mBJ-GGA oriented band structures are presented as supplementary figure S8a–c, respectively. With both the potential schemes, calculated minimum bandgap (E_g) of each specimen is given in table 4.

Calculations show direct bandgap semiconductor (Γ–Γ) features of CdSe and ZnSe irrespective of employed potential scheme and it is in concordance with respective experimental observations [1,24]. Though the computed fundamental bandgap (E_g) of CdSe and ZnSe with mBJ-GGA is almost identical to the respective experimental data [1,24], the same with PBE+U is smaller than the respective experimental data [1,24]. The HgSe under the mBJ-GGA scheme exhibits semiconductor character with narrow and direct bandgap (Γ–Γ). In contrast, the HgSe under the PBE+U scheme shows its metallic nature with coinciding valence band maximum and conduction band minimum along the high symmetry line (Γ–Γ). Though the former character of HgSe is supported by an experiment [4] and the latter one by another [3], calculations could not establish its experimentally observed semi-metal character with zero bandgap [2]. The discrepancy between mBJ-GGA based positive E_g and the corresponding experimental data is 0.363 eV [4], while the same between PBE+U based computed negative E_g and corresponding experimental data is nearly –0.12 eV [1,25].

From the aforesaid discussion, it is clear that though mBJ-GGA induced band structure and bandgap of CdSe and ZnSe are extremely close to the respective experimental observations, the same for the HgSe completely contradicts the corresponding experimental observation and its bandgap is found to be marginally positive. On the other hand, the PBE+U scheme is able to incorporate the interactions between localized *d*-electrons of transition metal elements and hence improve the accuracy of calculated electronic properties. In the present study, the PBE+U is successfully able to provide correct band structure and accurate bandgap of all the binary specimens. The PBE+U induced bandgaps of CdSe and ZnSe are only 0.132 and 0.197 eV, respectively, smaller than the corresponding mBJ-GGA induced data. The PBE+U also possesses a negative fundamental bandgap of HgSe, which agrees excellently well with the corresponding experimental observation. Moreover, though the qualitative nature of band structures of each ternary/quaternary alloy with both the potential schemes are almost identical, we have observed marginal discrepancy between the PBE+U and mBJ-GGA based computed bandgap data for each alloy. Therefore, the PBE+U potentials are able to show better performance compared to mBJ-GGA scheme in describing electronic properties of all the specimens within the $Cd_{1-x-y}Zn_xHg_ySe$ system.

3.4b *Density of states*: Calculations of density of states (DOS) for each quaternary alloy, especially the total (TDOS) for an alloy and the partial (PDOS) for its constituent atoms help us to achieve information regarding involvement of atomic orbitals constituting diverse electronic levels in different energy segments of respective band profile. Since calculated total and partial DOS profiles for mBJ-GGA and PBE+U become identical, the same for $Cd_{0.50}Zn_{0.25}Hg_{0.25}Se$, $Cd_{0.25}Zn_{0.50}Hg_{0.25}Se$ and $Cd_{0.25}Zn_{0.25}Hg_{0.50}Se$ quaternary alloys with the former potential scheme are presented as supplementary figure S9a–c, respectively. Electronic excitations between diverse electronic levels of valence and conduction band adjacent to Fermi level of band structure of a material are responsible for its different optical features. Therefore, the analyses of TDOS and hence PDOS of these regions have utmost importance. Close to the Fermi level, valence electronic states in the region from –2.5 to 0.0 eV comprises mostly Se-4p and marginally of Zn-3p, 3d; Cd-4p, 4d; Hg-5p, 5d states. The same in the conduction band region from 0.0 to 5.0 eV comprises mostly of Hg-7s, Zn-5s, Cd-6s and

Table 4. Calculated E_g (eV) for all the specimens with mBJ-GGA and PBE+U functional.

			E_g (eV)			
			Calculated			
x	*y*	Specimen	mBJ-GGA	PBE+U	Experimental data	Previous theoretical data
0.0	0.0	CdSe	1.849	1.719	1.90[a*], 1.82[b*]	0.45[a], 0.17[b1], 1.25[b2], 1.56[b3], 1.34[b4], 1.66[b5] 0.76[c1], 2.01[c2], 2.195[d1], 1.908[d2], 1.468[d3], 1.165[d4]
	0.25	$Cd_{0.75}Hg_{0.25}Se$	1.443	1.226		
	0.50	$Cd_{0.50}Hg_{0.50}Se$	1.007	0.721		
	0.75	$Cd_{0.25}Hg_{0.75}Se$	0.555	0.202		
	1.0	HgSe	0.057	–0.329	–0.205[a*], –0.20[c*] 0.42[d*]	–1.19[a], –1.23[b1], –0.60[b2], –0.50[b3], –0.50[b4], –0.40[b5], 1.635[d1], 1.426[d2], –0.38[d3], –0.55[d4], 0.10[e], 0.07[f],0.01[g], –0.55[h]
0.25	0.0	$Cd_{0.75}Zn_{0.25}Se$	2.051	1.934		
	0.25	$Cd_{0.50}Zn_{0.25}Hg_{0.25}Se$	1.658	1.446		
	0.50	$Cd_{0.25}Zn_{0.25}Hg_{0.50}Se$	1.248	0.936		
	0.75	$Zn_{0.25}Hg_{0.75}Se$	0.817	0.437		
0.50	0.0	$Cd_{0.50}Zn_{0.50}Se$	2.306	2.167		
	0.25	$Cd_{0.25}Zn_{0.50}Hg_{0.25}Se$	1.925	1.691		
	0.50	$Zn_{0.50}Hg_{0.50}Se$	1.532	1.199		
0.75	0.0	$Cd_{0.25}Zn_{0.75}$ Se	2.583	2.398		
	0.25	$Zn_{0.75}Hg_{0.25}Se$	2.223	1.951		
1.0	0.0	ZnSe	2.842	2.645	2.82[a*], 2.87[b*]	1.39[a], 0.88[b1], 2.24[b2] 2.58[b3], 2.33[b4], 2.68[b5] 1.45[c1], 2.84[c2], 2.641[d1], 2.267[d2], 2.101[d3], 1.701[d4], 2.81[e]

Experimental data: [a*][1], [b*][24], [c*][25], [d*][4].

Previous theoretical data: [a][27] = GDSP/DFT, [b1][43] = LDA, [b2][43] = GW, [b3][43] = G′W′, [b4][43] = GWΓ, [b5][43] = G′W′Γ, [c1][44] = LDA, [c2][44] = GW, [d1][45] = NRL+LDA+EV, [d2][45] = NRL+GGA+EV, [d3][45] = RL+LDA+EV, [d4][45] = RL+GGA+EV, [e][62] = mBJ, [f][35] = mBJ, [g][36] = mBJ, [h][38] = EV-GGA.

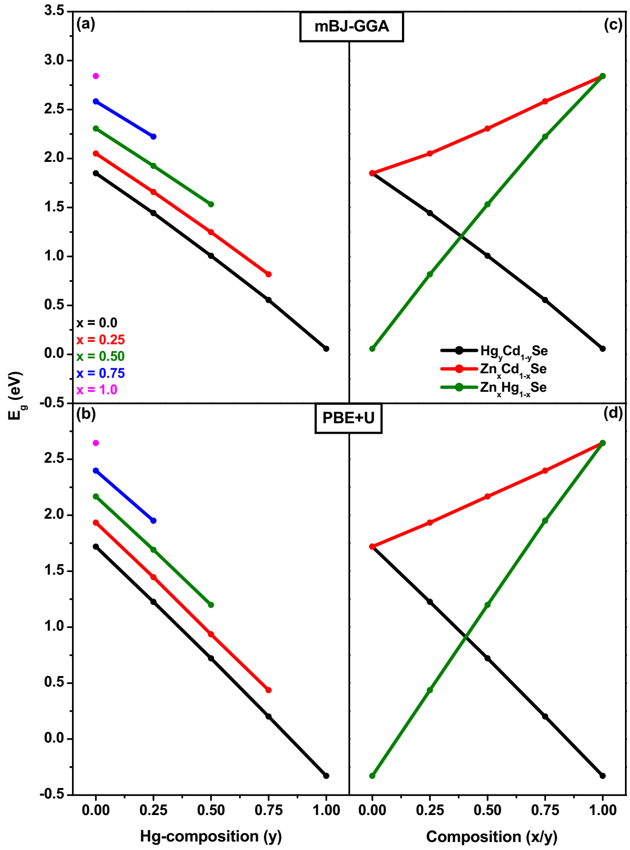

Figure 6. (**a**) Hg-composition (y) dependence curves of mBJ-GGA based computed E_g for the compounds under $Cd_{1-x-y}Zn_xHg_ySe$ quaternary system. (**b**) Hg-composition (y) dependence curves of PBE+U based computed E_g for the compounds under $Cd_{1-x-y}Zn_xHg_ySe$ quaternary system. (**c**) Composition (x or y) dependence curves of mBJ-GGA based computed E_g for the ternary alloys. (**d**) Composition (x or y) dependence curves of PBE+U based computed E_g for the ternary alloys.

Se-4p, 5s, 4d states. Therefore, diverse optical features of considered compounds and alloys are resulting from highly probable electronic excitations from the filled Se-4p valence state to vacant Hg-7s, Cd-6s and Zn-5s states of conduction band nearest to the Fermi level.

3.4c *Concentration dependence of bandgap*: In the case of $Cd_{1-x-y}Zn_xHg_ySe$ system and with mBJ-GGA and PBE+U, reduction in calculated E_g with growing mercury concentration (y) at each considered zinc concentration (x) are displayed in figure 6a and b, respectively. But, calculated E_g with both the potential schemes enhances with growing zinc concentration (x) at any particular mercury concentration (y). Calculated E_g nonlinearly increases with growing zinc concentration (x) in $Zn_xCd_{1-x}Se$ and $Zn_xHg_{1-x}Se$ ternary systems, but reduces in the $Hg_yCd_{1-y}Se$ ternary system with growing mercury composition (y). For mBJ-GGA and PBE+U schemes, such variations in the ternary systems are presented in figure 6c and d, respectively. In case of these ternary systems, the following quadratic equations express the nonlinear variation in E_g (x) or $E_g(y)$ curve

$$E_g^{\mathrm{ZnCdSe}}(x) = xE_g^{\mathrm{ZnSe}} + (1-x)E_g^{\mathrm{CdSe}} - x(1-x)b_g^{\mathrm{ZnCdSe}} \tag{6}$$

$$E_g^{\mathrm{HgCdSe}}(x) = xE_g^{\mathrm{HgSe}} + (1-x)E_g^{\mathrm{CdSe}} - x(1-x)b_g^{\mathrm{HgCdSe}} \tag{7}$$

$$E_g^{\mathrm{ZnHgSe}}(x) = xE_g^{\mathrm{ZnSe}} + (1-x)E_g^{\mathrm{HgSe}} - x(1-x)b_g^{\mathrm{ZnHgSe}} \tag{8}$$

In the $Zn_xCd_{1-x}Se$ system, the $E_g(x)$ curve shows marginal downward deviation from its ideal linear variation and calculated bandgap bowing parameter is $b_g^{\mathrm{ZnCdSe}} = 0.1554$ eV with mBJ-GGA and 0.0709 eV with PBE+U scheme. In contrast, marginal upward deviation from ideal linear variation with any XC potential is observed in the $E_g(y)$ curve of the $Hg_yCd_{1-y}Se$ as well as in the $E_g(x)$ curve of the $Zn_xHg_{1-x}Se$ system. Our calculated mBJ-GGA based bandgap bowing parameter for $Hg_yCd_{1-y}Se$ and $Zn_xHg_{1-x}Se$ system is $b_g^{\mathrm{HgCdSe}} = -0.2286$ eV and $b_g^{\mathrm{ZnHgSe}} = -0.3497$ eV, respectively, while the same with the PBE+U potentials is $b_g^{\mathrm{HgCdSe}} = -0.1029$ eV and $b_g^{\mathrm{ZnHgSe}} = -0.1760$ eV, respectively.

3.4d *Effective mass of charged particles*: The mass (m^*) of an accelerated charged particle due to periodically varying potential is called its effective mass. Therefore, free-particle mass (m_0) and effective mass (m^*) of a particle are completely different from each other. It provides information regarding the nature of dominant carriers (electron or hole) accountable for transport properties exhibited by a semiconductor. Table 5 contains computed effective mass of electrons (m_e^*/m_0), heavy-hole (m_{hh}^*/m_0), and light hole (m_{lh}^*/m_0) of each specimen (in the unit of m_0). We have observed m^*(mBJ-GGA)>m^*(PBE+U) in the case of each specimen. Clearly, m_{hh}^*/m_0 and m_{lh}^*/m_0 of any sample is larger than the corresponding m_e^*/m_0. Therefore, the transport phenomenon in any considered specimen is due to the predominant role of electrons compared to the holes. In the $Cd_{1-x-y}Zn_xHg_ySe$ system, m_e^*/m_0, m_{lh}^*/m_0 and m_{hh}^*/m_0 reduces with growing mercury concentration (y) at each considered zinc concentration (x). On the other hand, each of them enhances with growing zinc concentration (x) at any particular mercury concentration (y). We have displayed such variations with mBJ-GGA as supplementary figure S10a–c and the same with PBE+U as supplementary figure S10d–f, respectively.

3.5 *Optical properties*

3.5a *Frequency dependence of diverse optical parameters*: Optical characteristics of each specimen allied to the

Table 5. Effective mass of electron (m_e^*), heavy hole (m_{hh}^*) and light hole (m_{lh}^*) in unit free electron mass (m_0) for all the specimens with mBJ-GGA and PBE+U functional.

			Hole effective mass			
	Electron effective mass (m_e^*/m_0)		Heavy hole (m_{hh}^*/m_0)		Light hole (m_{lh}^*/m_0)	
Compounds	mBJ-GGA	PBE+U	mBJ-GGA	PBE+U	mBJ-GGA	PBE+U
CdSe	0.272	0.231	1.254	1.121	0.444	0.366
$Cd_{0.75}Hg_{0.25}Se$	0.265	0.229	1.219	1.108	0.433	0.358
$Cd_{0.50}Hg_{0.50}Se$	0.257	0.225	1.193	1.086	0.421	0.347
$Cd_{0.25}Hg_{0.75}Se$	0.251	0.221	1.149	1.072	0.407	0.342
HgSe	0.243	0.215	1.111	1.045	0.395	0.330
$Cd_{0.75}Zn_{0.25}Se$	0.301	0.251	1.344	1.171	0.529	0.438
$Cd_{0.50}Zn_{0.25}Hg_{0.25}Se$	0.291	0.249	1.306	1.154	0.515	0.419
$Cd_{0.25}Zn_{0.25}Hg_{0.50}Se$	0.281	0.245	1.275	1.133	0.495	0.407
$Zn_{0.25}Hg_{0.75}Se$	0.275	0.238	1.233	1.109	0.472	0.395
$Cd_{0.50}Zn_{0.50}Se$	0.328	0.272	1.441	1.221	0.608	0.495
$Cd_{0.25}Zn_{0.50}Hg_{0.25}Se$	0.319	0.268	1.407	1.205	0.586	0.481
$Zn_{0.50}Hg_{0.50}Se$	0.311	0.262	1.363	1.181	0.559	0.468
$Cd_{0.25}Zn_{0.75}$ Se	0.355	0.293	1.527	1.265	0.671	0.566
$Zn_{0.75}Hg_{0.25}Se$	0.347	0.285	1.479	1.239	0.646	0.544
ZnSe	0.392	0.315	1.628	1.311	0.758	0.643

$Cd_{1-x-y}Zn_xHg_ySe$ system are analysed by calculating mBJ-GGA and PBE+U based frequency response spectra of different optical parameters up to 30.0 eV of incident photon energy. The optical properties of any material are analysed mainly in terms of its complex dielectric function $\varepsilon(\omega)$ and it provides complete behaviour of any compound during its interaction with the incident electromagnetic radiation. The expressions for real part of dielectric function $\varepsilon_1(\omega)$, imaginary part of dielectric function $\varepsilon_2(\omega)$, refractive index $n(\omega)$, extinction coefficient $k(\omega)$, normal incidence reflectivity $R(\omega)$, optical conductivity $\sigma(\omega)$, optical absorption coefficient $\alpha(\omega)$, electron energy loss function $L(\omega)$ and optical transmission coefficient $T(\omega)$, used in the present study, are provided in Section-II of supplementary materials.

The real part $\varepsilon_1(\omega)$ describes the dispersion and the imaginary part $\varepsilon_2(\omega)$ describes the energy absorption of the incident electromagnetic radiation by the material. A material behaves as an optically rarer medium when its refractive index is greater than unity. It behaves as fully transparent material when the refractive index becomes unity. The negative value of refractive index makes a material optically denser and hence behaves as an opaque material. A material having higher extinction or attenuation coefficient offers higher resistance to the incident photons to penetrate through the material and vice versa. For calculation of reflection losses from optical instruments, it is necessary to calculate the reflectivity at normal incidence. The normal incidence reflectivity depends upon refractive indices of two mediums. Optical conductivity is the property of a material that gives the relationship between the induced current density in the material and the magnitude of the inducing electric field for arbitrary frequencies. Therefore, significantly high optical conductivity of a material implies its metallic behaviour and vice versa. The optical absorption coefficient $\alpha(\omega)$ is the measurement of the length penetrated by an incident photon inside a semiconductor material before its complete absorption when its associated energy is greater than roughly the electronic bandgap of the material. Electron energy loss function of a material is useful in calculating energy loss due to inelastic scattering of electrons by atoms in a lattice and its frequency response is opposite to the $\varepsilon_2(\omega)$ of that material. Optical transmission refers to the proportion of light that is transmitted through an optically clear medium. Applications such as fibre-optic communications, optoelectronic sensors and photonics require the highest levels of transmission.

For $Cd_{0.50}Zn_{0.25}Hg_{0.25}Se$, $Cd_{0.25}Zn_{0.25}Hg_{0.50}Se$ and $Cd_{0.25}Zn_{0.50}Hg_{0.25}Se$ quaternary alloys, the variation of $\varepsilon_1(\omega)$, $\varepsilon_2(\omega)$, $n(\omega)$, $k(\omega)$, with frequency of the incident radiation under the mBJ-GGA are displayed as figure 7a–d and with PBE+U as figure 7e–h, respectively. On the other hand, variation of $R(\omega)$, $\sigma(\omega)$, $\alpha(\omega)$, $L(\omega)$ with frequency of the incident radiation under the mBJ-GGA are displayed as figure 8a–d and with PBE+U as figure 8e–h, respectively. Moreover, dependence of each optical parameter on wavelength (λ) of the incident photon energy is displayed as inset in the corresponding frequency dependence spectra. They exhibit contributions of these optical parameters in the UV–Vis and IR regions. Mutual frequency dependence of transmission coefficient $T(\omega)$ and absorption edge $\alpha(\omega)$ in

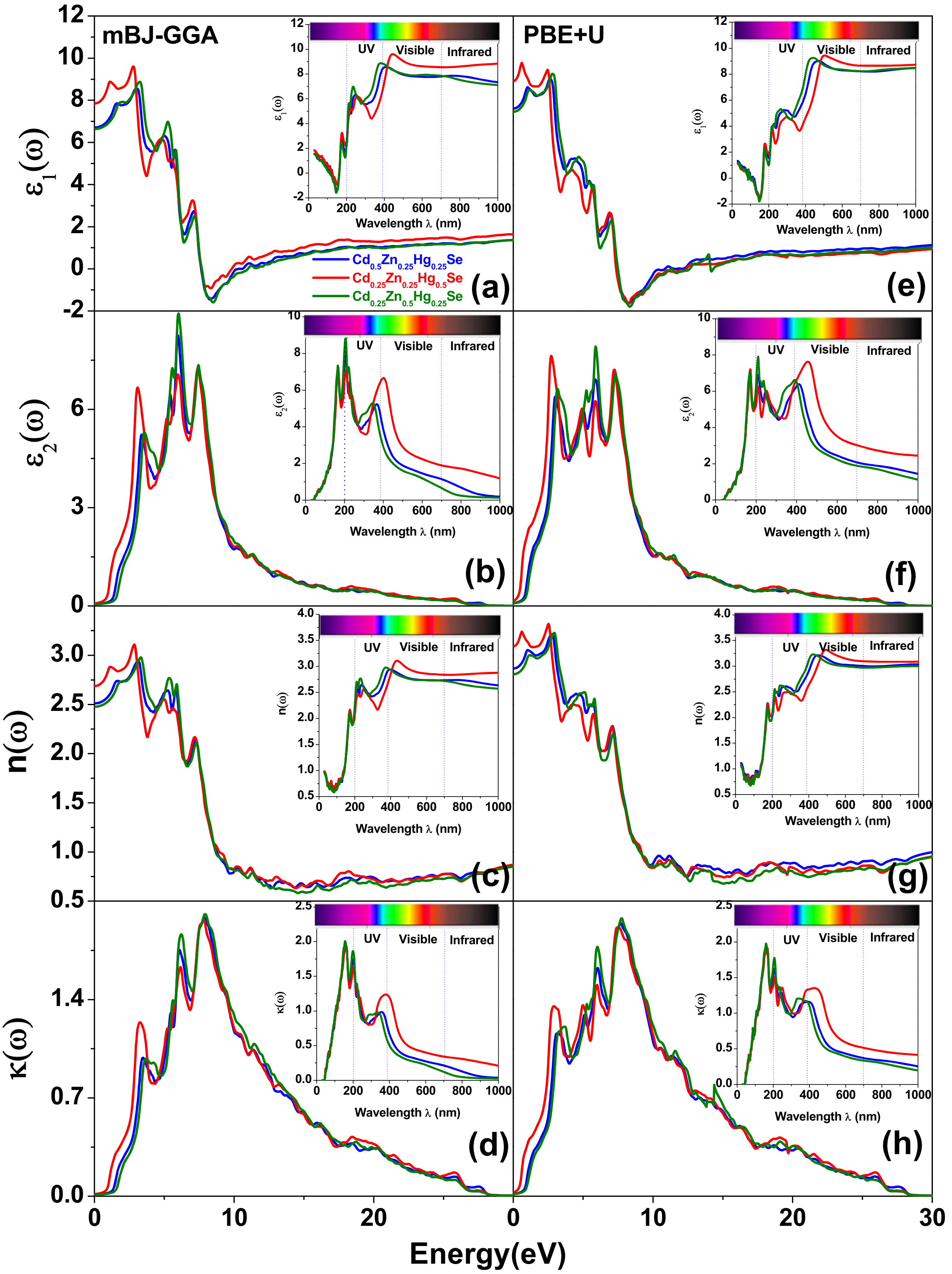

Figure 7. Computed frequency response spectra of (**a**) $\varepsilon_1(\omega)$, (**b**) $\varepsilon_2(\omega)$, (**c**) $n(\omega)$, (**d**) $k(\omega)$ with mBJ-GGA and (**e**) $\varepsilon_1(\omega)$, (**f**) $\varepsilon_2(\omega)$, (**g**) $n(\omega)$, (**h**) $k(\omega)$ with PBE+U for the quaternary alloys. The variation of each optical parameter with wavelength is displayed as inset.

case of quaternary alloys under mBJ-GGA and PBE+U are displayed in figure 9a and b, respectively. Diverse optical constants of each specimen are calculated and presented. Though frequency dependence of any optical feature of a specimen is qualitatively similar to that with PBE+U, they cater quantitatively to different optical constants.

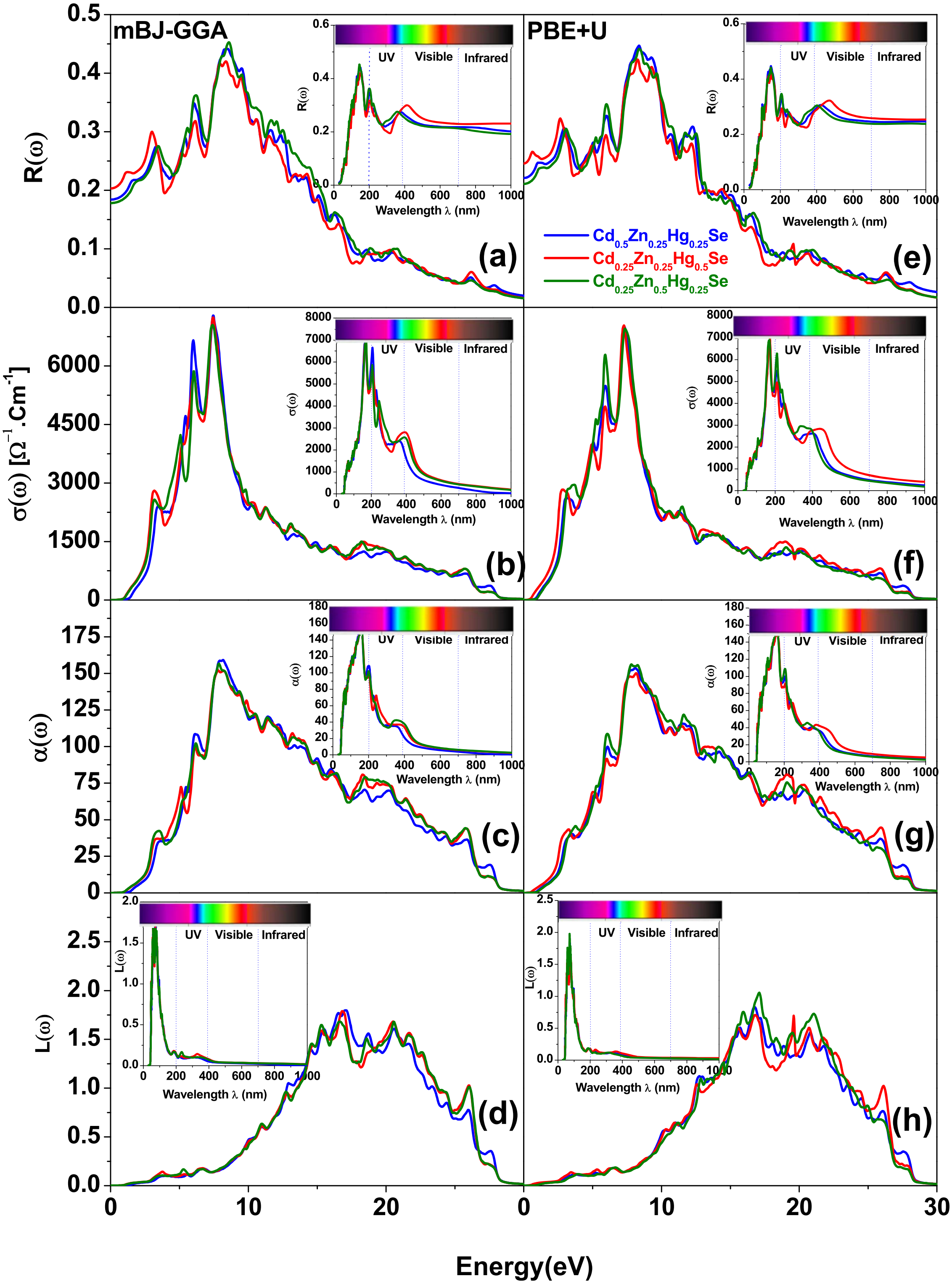

Figure 8. Computed frequency response spectra of (**a**) *R*(ω), (**b**) *σ*(ω), (**c**) α(ω), (**d**) *L*(ω) with mBJ-GGA and (**e**) *R*(ω), (**f**) *σ*(ω), (**g**) α(ω), (**h**) *L*(ω) with PBE+U for the quaternary alloys. The variation of each optical parameter with wavelength is displayed as inset.

The $\varepsilon_1(\omega)$ spectra of each quaternary specimen show peaks and hence prominent dispersion of incident radiation below 5.0 eV, while negative $\varepsilon_1(\omega)$ ensures their metallic character in 7.5–12.0 eV energy region. The $\varepsilon_2(\omega)$ spectra of each quaternary specimen show peaks in the 3.0–9.0 eV energy region and they originate as a result of collective effort of

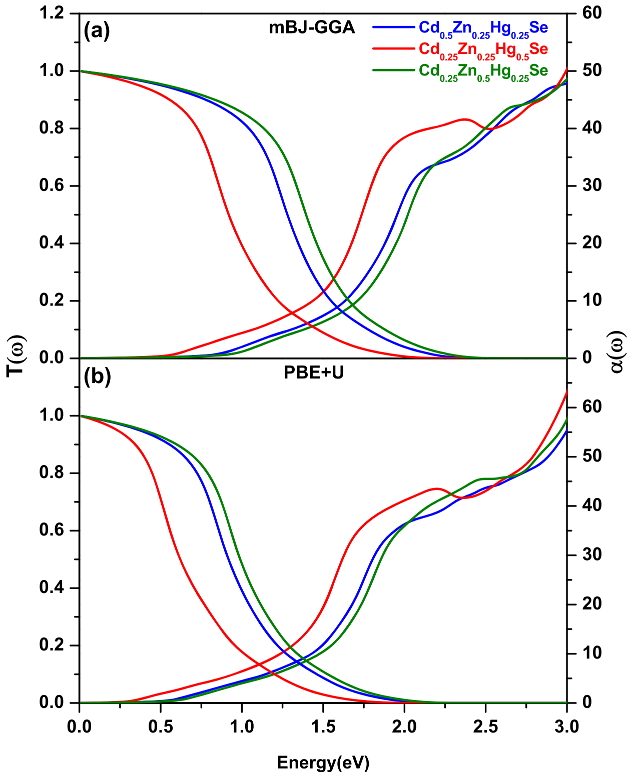

Figure 9. Mutual variation of computed frequency response spectra of transmission coefficient $T(\omega)$ and absorption edge $\alpha(\omega)$ of the $Cd_{0.50}Zn_{0.25}Hg_{0.25}Se$, $Cd_{0.25}Zn_{0.50}Hg_{0.25}Se$ and $Cd_{0.25}Zn_{0.25}Hg_{0.50}Se$ quaternary alloys with (**a**) mBJ-GGA and (**b**) PBE+U potentials.

electronic transitions from filled Se-4p valence state to empty Hg-7s, Zn-5s, Cd-6s states of conduction band.

The $n(\omega)$ spectra of each quaternary specimen show the largest refractive index $n(\omega)_{max}$ in the incident photon energy region below 8.0 eV. The $n(\omega)_{max}$ for $Cd_{0.50}Zn_{0.25}Hg_{0.25}Se$, $Cd_{0.25}Zn_{0.25}Hg_{0.50}Se$ and $Cd_{0.25}Zn_{0.50}Hg_{0.25}Se$ quaternary alloy is calculated as 2.940, 3.109 and 2.978, respectively, with mBJ-GGA, and 3.213, 3.318 and 3.229, respectively, with PBE+U. Above 9.0 eV, the $n(\omega)$ for each specimen below unity ($c/v<1$) is a signature of opacity of each material and it ensures larger group velocity of wave packet through the semiconductor specimens $v_g = c/n$ than the velocity of light (c) in free-space [84]. Significantly high $k(\omega)$ with peaks is observed in the $k(\omega)$ spectra of the quaternary alloys in the energy region 3.0–13.0 eV and the peak value $k_{max}(\omega)$ for all the specimens is very close to 2.0. It indicated that extremely high resistance is offered by these semiconductor specimens to those photons having energy in the 3.0–13.0 eV compared to the photons having energy beyond this range [84].

Considerably high reflectivity [$R(\omega)>0.20$] in the wide energy range 0.0–15.0 eV is observed in the $R(\omega)$ spectra of each quaternary specimen. Few peaks exist in this energy region with maximum reflectivity $R_{max}(\omega) > 0.40$. We have observed a substantially high $\sigma(\omega)$ having a pair of peaks in the narrow energy range 5.5–8.5 eV in the $\sigma(\omega)$ spectra of the quaternary alloys and it ensures metallic character of quaternary specimens in this energy region. Computed $\sigma_{max}(\omega)$, i.e., largest optical conductivity for the $Cd_{0.50}Zn_{0.25}Hg_{0.25}Se$, $Cd_{0.25}Zn_{0.25}Hg_{0.50}Se$ and $Cd_{0.25}Zn_{0.50}Hg_{0.25}Se$ specimen with mBJ-GGA are 7290, 7242 and 7050 $(\text{Ohm cm})^{-1}$, respectively, and with PBE+U are 7000, 7036 and 6951 $(\text{Ohm cm})^{-1}$, respectively. The $\alpha(\omega)$ of each quaternary specimen becomes substantially high with peaks having significant intensity in the region 7.0–10.0 eV in the respective $\alpha(\omega)$ spectra. The $\alpha_{max}(\omega)$, i.e., maximum absorption of incident energy by the three quaternary specimens exist in between 150 and 160 cm^{-1}.

It is observed that the frequency responses of the electronic energy loss function $L(\omega)$ and $\varepsilon_2(\omega)$ of a specimen are opposite in nature. Each quaternary specimen shows negligibly small $L(\omega)$ but significantly high $\varepsilon_2(\omega)$ up to 10.0 eV of energy. Conversely, $L(\omega)$ of each specimen becomes significantly high with distinct peaks but $\varepsilon_2(\omega)$ becomes negligibly small in the energy region 12.0–26.0 eV. For each specimen, plasma resonance frequency is the frequency corresponding to the energy at which a peak with maximum intensity in the corresponding $L(\omega)$ spectrum occurs.

Figure 9a and b shows significantly high transmission coefficient $T(\omega)$ of any quaternary alloy with mBJ-GGA and PBE+U, respectively, in comparison with respective reflection and absorption coefficients in the extremely low energy region. Conversely, significantly, dominating absorption compared to the reflection and transmission is observed in the high-energy region. Nearly equally intense absorption, transmission and reflection take place simultaneously in the 1.0–1.5 eV narrow energy region.

3.5b *Optical constants*: The static dielectric constant $\varepsilon_1(0)$, refractive index $n(0)$ and reflectivity $R(0)$ for each specimen are calculated from the corresponding spectra and presented in table 6. Each of them shows strong bandgap dependence. In a semiconductor, the $\varepsilon_1(0)$ changes approximately as a function of bandgap according to the Penn model [85] in the following way:

$$\varepsilon_1(0) \approx 1 + \left(\frac{\hbar\omega_P}{E_g}\right)^2 \qquad (9)$$

Moreover, static refractive index and static reflectivity of a semiconductor are connected with its $\varepsilon_1(0)$ as $n(0) \approx \sqrt{\varepsilon_1(0)}$ and $R(0) = [1 - n(0)]^2/[1 + n(0)]^2$. Therefore, a semiconductor with larger minimum bandgap (E_g) possesses a smaller value of static optical constants and vice versa. Calculated static optical constants of the specimens increases according to table 6, while the corresponding E_g reduces in table 4 with growing mercury concentration (y) at each considered zinc concentration (x). A completely reverse picture is observed with growing zinc composition (x) at each particular mercury composition (y). These

Table 6. Calculated zero-frequency limits for all the specimens with mBJ-GGA and PBE+U functional.

			Zero-frequency limit					
			$\varepsilon_{1(0)}$		$n(0)$		$R(0)$	
x	y	Specimen	mBJ-GGA	PBE+U	mBJ-GGA	PBE+U	mBJ-GGA	PBE+U
0.0	0.0	CdSe	5.903	6.543	2.388	2.693	0.177	0.209
			5.8[a*], 5.06[c]					
	0.25	$Cd_{0.75}Hg_{0.25}Se$	6.803	7.758	2.551	2.918	0.192	0.231
	0.50	$Cd_{0.50}Hg_{0.50}Se$	7.938	9.092	2.734	3.146	0.212	0.257
	0.75	$Cd_{0.25}Hg_{0.75}Se$	9.441	10.541	2.925	3.398	0.236	0.285
	1.0	HgSe	11.301	12.221	3.148	3.654	0.272	0.316
			11.24[a], 10.74[b], 16.65[c]	3.27[a]	0.283[a], 0.284[b]			
0.25	0.0	$Cd_{0.75}Zn_{0.25}Se$	5.838	6.454	2.356	2.646	0.170	0.200
	0.25	$Cd_{0.50}Zn_{0.25}Hg_{0.25}Se$	6.706	7.608	2.511	2.866	0.184	0.221
	0.50	$Cd_{0.25}Zn_{0.25}Hg_{0.50}Se$	7.849	8.911	2.687	3.091	0.203	0.246
	0.75	$Zn_{0.25}Hg_{0.75}Se$	9.305	10.341	2.877	3.345	0.227	0.273
0.50	0.0	$Cd_{0.50}Zn_{0.50}Se$	5.774	6.352	2.321	2.598	0.164	0.191
	0.25	$Cd_{0.25}Zn_{0.50}Hg_{0.25}Se$	6.633	7.455	2.477	2.808	0.178	0.211
	0.50	$Zn_{0.50}Hg_{0.50}Se$	7.759	8.708	2.642	3.037	0.195	0.235
0.75	0.0	$Cd_{0.25}Zn_{0.75}Se$	5.747	6.254	2.279	2.546	0.156	0.183
	0.25	$Zn_{0.75}Hg_{0.25}Se$	6.522	7.261	2.427	2.748	0.169	0.201
1.0	0.0	ZnSe	5.704	6.153	2.247	2.484	0.148	0.176
			5.9[a*]	2.34[a]	0.158[a]			
			5.51[a], 5.39[c]					

Experimental data: [a*][26].
Previous theoretical data: [a][62], [b][35], [c][45].

changes in mBJ-GGA based $\varepsilon_1(0)$, $n(0)$ and $R(0)$ are presented as supplementary figure S11a–c and with PBE+U as supplementary figure S11d–f, respectively. Moreover, each of the PBE+U based computed optical constants of any specimen is higher than the respective mBJ-GGA based data, while the bandgap with the latter is higher than that with the former. In case of CdSe and ZnSe, available experimentally observed $\varepsilon_1(0)$ [26] are extremely close to the mBJ-GGA based corresponding calculated data.

In $\varepsilon_2(\omega)$, $k(\omega)$, $\sigma(\omega)$ and $\alpha(\omega)$ spectrum, critical point energy (E_c) is the minimum incident energy needed to initiate interaction between these parameters and incident radiation in a material. Our calculated E_c for all the specimens are presented in table 7 and each of them shows strong bandgap dependence. Calculated E_c in each of the $\varepsilon_2(\omega)$, $k(\omega)$, $\sigma(\omega)$ and $\alpha(\omega)$ spectra of the compounds in table 7 and their calculated E_g in table 4 decrease with growing mercury concentration (y) at each considered zinc concentration (x). A completely reverse picture is observed with growing zinc composition (x) at each considered mercury composition (y). These type of variation in mBJ-GGA based computed E_c in the $\varepsilon_2(\omega)$, $k(\omega)$, $\sigma(\omega)$ and $\alpha(\omega)$ spectra are presented as supplementary figure S12a–d and with PBE+U as supplementary figure S12e–h, respectively. Moreover, the mBJ-GGA based calculated E_g of a specimen and calculated E_c in its any of the said spectra is higher than the PBE+U based respective data. The Kramers–Kronig transformations between $\varepsilon_1(\omega)$ and $\varepsilon_2(\omega)$, between $n(\omega)$ and $k(\omega)$ as well as the relation $\sigma(\omega) = \omega\varepsilon_2(\omega)/4\pi$ and $\alpha(\omega) = 2\omega k(\omega)/c$ [84] authenticate the similarity in the compositional variation of calculated bandgap E_g and that of calculated E_c in the $\varepsilon_2(\omega)$, $k(\omega)$, $\sigma(\omega)$ and $\alpha(\omega)$ spectra, respectively, and vice versa.

3.5c *Oscillator strength*: For $Cd_{0.50}Zn_{0.25}Hg_{0.25}Se$, $Cd_{0.25}Zn_{0.25}Hg_{0.50}Se$ and $Cd_{0.25}Zn_{0.50}Hg_{0.25}Se$ quaternary alloys, it is calculated with the effective number of electrons (N_{eff}) reaching their respective conduction band at the time of any highest occupied molecular orbital–lowest unoccupied molecular orbital optical transition. With mBJ-GGA, variation of oscillator strength (N_{eff}) of each quaternary alloy with incident energy is presented in figure 10. No electron is able to reach the conduction band ($N_{eff} = 0$) of any quaternary alloy with incident energy smaller than the respective bandgap. However, electrons start reaching the conduction band when incident energy is nearly close to the bandgap of the material. The oscillator strength (N_{eff}) for each specimen sharply increases with increasing incident energy. Beyond 26.0 eV of incident energy, we have observed saturation in the oscillator strength. It is indicating the maximum oscillator strength (N_{eff}) shown by the respective quaternary alloy during an optical excitation. We have observed that at saturation, the available N_{eff} in the conduction band is 40, 41 and 38 for $Cd_{0.50}Zn_{0.25}Hg_{0.25}Se$,

Table 7. Calculated critical points for all the specimens with mBJ-GGA and PBE+U functional.

			Critical points (eV) in the spectra of							
			$\varepsilon_2(\omega)$		$k(\omega)$		$\sigma(\omega)$		$\alpha(\omega)$	
x	*y*	Specimen	mBJ	PBE+U	mBJ	PBE+U	mBJ	PBE+U	mBJ	PBE+U
0.0	0.0	CdSe	1.781	1.411	1.631	1.361	1.870	1.476	1.986	1.321
	0.25	$Cd_{0.75}Hg_{0.25}Se$	1.312	1.015	1.162	0.965	1.401	1.080	1.517	0.925
	0.50	$Cd_{0.50}Hg_{0.50}Se$	0.884	0.629	0.734	0.579	0.973	0.694	1.089	0.539
	0.75	$Cd_{0.25}Hg_{0.75}Se$	0.467	0.259	0.317	0.209	0.556	0.324	0.672	0.169
	1.0	HgSe	0.039	–0.108	–0.111	–0.158	0.128	–0.04	0.244	–0.198
0.25	0.0	$Cd_{0.75}Zn_{0.25}Se$	2.135	1.681	1.982	1.629	2.221	1.753	2.344	1.598
	0.25	$Cd_{0.50}Zn_{0.25}Hg_{0.25}Se$	1.656	1.261	1.503	1.209	1.742	1.333	1.865	1.178
	0.50	$Cd_{0.25}Zn_{0.25}Hg_{0.50}Se$	1.189	0.875	1.036	0.823	1.275	0.947	1.398	0.792
	0.75	$Zn_{0.25}Hg_{0.75}Se$	0.739	0.493	0.586	0.441	0.825	0.565	0.948	0.410
0.50	0.0	$Cd_{0.50}Zn_{0.50}Se$	2.397	1.932	2.246	1.882	2.485	2.003	2.611	1.858
	0.25	$Cd_{0.25}Zn_{0.50}Hg_{0.25}Se$	1.955	1.526	1.804	1.476	2.043	1.597	2.169	1.452
	0.50	$Zn_{0.50}Hg_{0.50}Se$	1.491	1.181	1.340	1.131	1.579	1.252	1.705	1.107
0.75	0.0	$Cd_{0.25}Zn_{0.75}$ Se	2.822	2.182	2.667	2.134	2.911	2.252	3.024	2.103
	0.25	$Zn_{0.75}Hg_{0.25}Se$	2.298	1.791	2.143	1.740	2.387	1.861	2.514	1.712
1.0	0.0	ZnSe	3.281	2.432	3.132	2.387	3.371	2.501	3.479	2.362

$Cd_{0.25}Zn_{0.25}Hg_{0.50}Se$ and $Cd_{0.25}Zn_{0.50}Hg_{0.25}Se$ quaternary alloy, respectively.

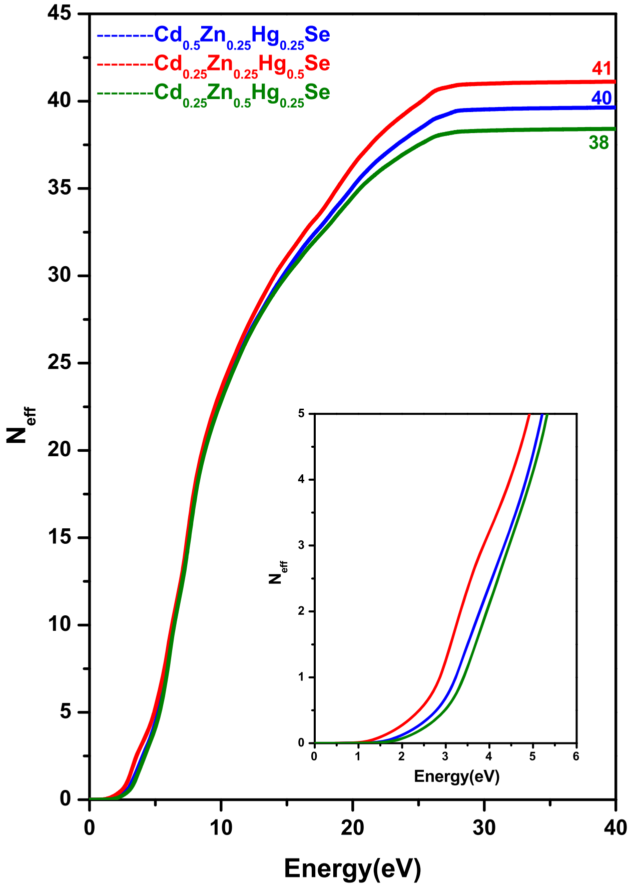

Figure 10. Computed mBJ-GGA based oscillator strength (N_{eff}) *vs.* incident energy curve for the $Cd_{0.50}Zn_{0.25}Hg_{0.25}Se$, $Cd_{0.25}Zn_{0.50}Hg_{0.25}Se$ and $Cd_{0.25}Zn_{0.25}Hg_{0.50}Se$ quaternary alloys. The magnified view of variation of N_{eff} with energy of the incident photon is displayed as inset for low energy region 0.0–6.0 eV.

4. Conclusion

The present first-principle calculations on cubic compounds and alloys under the $Cd_{1-x-y}Zn_xHg_ySe$ triangular quaternary system show that each of them exhibits thermodynamic and mechanical stability, ductility, elastic anisotropy and compressibility. Majority of covalent character over ionic is observed in the chemical bonding of each specimen. Bending in chemical bonds shows superiority over stretching in each specimen. In each specimen, inter-atomic forces are observed to be central in nature. Though zinc-blende binary compounds are dynamically stable, ternary and quaternary alloys in zinc-blende phase show dynamical instability. Therefore, mechanical stability, but dynamical instability is indicating zinc-blend as a meta-stable phase of the ternary and quaternary alloys. Calculations of Debye temperature, thermal conductivity and melting temperature of each specimen are also a part of the present study. Irrespective of nature of the employed XC potential scheme, ZnSe, CdSe and any kind of alloy are direct ($\Gamma-\Gamma$) fundamental bandgap semiconductor. Computations with PBE+U confirm the metallic character of HgSe, while mBJ-GGA reveals its semiconductor character with narrow and direct ($\Gamma-\Gamma$) bandgap. The mBJ-GGA scheme provides a comparatively larger bandgap of any specimen compared to the PBE+U. Transport phenomenon in any considered specimen is due to the predominant role of electrons having lower effective mass compared to the holes. The peaks having significant intensity in the spectrum of dielectric function of any considered sample originate from Se-4p to Zn-5s, Cd-6s and Hg-7s electronic transitions. Semiconductors with superior bandgap possesses lower static optical constants, while they require greater threshold energies (E_c) to initiate response in the $\varepsilon_2(\omega)$, $k(\omega)$, $\sigma(\omega)$ and $\alpha(\omega)$ spectra and vice versa. The availability of sufficient amount of electrons in the conduction band of any quaternary alloy during any optical excitation is ensured beyond 26.0 eV of incident energy with respective computed oscillator strength.

Based on calculated mechanical properties, e.g., strength/hardness, ductility, anisotropy, compressibility, etc., the cubic specimens allied to the $Cd_{1-x-y}Zn_xHg_ySe$ system would be suitable for load deflection, thermo-elastic stress, etc., related mechanical applications. Computed thermal properties, e.g., thermal conductivity and melting temperature reveal that they would be potential materials for thermal resistant coating, thermal barrier and thermal management-related applications.

Zinc-blende ternary and quaternary semiconductors of the $Cd_{1-x-y}Zn_xHg_ySe$ system possess direct fundamental bandgap (Γ–Γ). Optical properties of these alloys are regulated by their respective direct bandgap centred at Γ-point. Transport properties in these alloys are predominantly due to electrons and they exhibit high mobility. Moreover, substantial variation of the fundamental optical absorption edge of these alloys is observed over the near-UV and UV ranges of the electromagnetic spectrum with concentrations x and y. Such striking optoelectronic features properties of these semiconductor alloys would lead them as potential candidates in diverse near-UV and UV optoelectronic applications.

Acknowledgements

The DST-INSPIRE-SRF [Ref. No DST/INSPIRE/03/2017/002068] of the DST, Government of India, is gratefully acknowledged by Sayantika Chanda.

References

[1] Medelung O (ed) 1982 *Landolt Bornstein: numerical data and functional relationship in science and technology* (Springer)

[2] Von Truchseβ M, Pfeuffer-Jeschke A, Becker C R, Landwehr G and Batke E 2000 *Phys. Rev. B* **61** 1666

[3] Szuszkiewi W 1979 *Phys. Status Solidi (b)* **91** 361

[4] Gawlik K U, Kipp L, Skibowski M, Orłowski N and Manzke R 1997 *Phys. Rev. Lett.* **78** 3165

[5] Wang J and Isshiki M 2006 *Wide-bandgap II–VI semiconductors: growth and properties, Springer handbook of electronic and photonic materials* (Berlin: Springer) p 325

[6] Hasse M A, Qui J, De Puydt J M and Cheng H 1991 *Appl. Phys. Lett.* **59** 1272

[7] Tamargo M C, Brasil M J S P, Nahory R E, Martin R J, Weaver A L and Gilchrist H L 1991 *Semicond. Sci. Technol.* **6** A8

[8] Shieh F, Saunders A E and Korgel B A 2005 *J. Phys. Chem. B* **109** 8538

[9] Peng Z A and Peng X G 2001 *J. Am. Chem. Soc.* **123** 183

[10] Xi L F, Chua K H, Zhao Y Y, Zhang J, Xiong Q H and Lam Y M 2012 *RSC Adv.* **2** 5243

[11] Wissmann H, Tran-Anh T, Rogaschewski S and von Ortenberg M 1990 *J. Cryst. Growth* **201/202** 619

[12] Kuno M, Higginson K A, Bonevich J E, Qadri S B, Yousuf M and Mattoussi H 2002 *Proc. SPIE* **4808** 146

[13] Esmaeili-Zare M, Salavati-Niasari M and Sobhani A 2012 *Ultrason. Sonochem.* **19** 1079

[14] Bazarganipour M, Sadri M, Davar F and Salavati-Niasari M 2011 *Polyhedron* **30** 1103

[15] Medelung O (ed) 1996 *Landolt Bornstein: semiconductors basic data in science & technology* (Berlin: Springer)

[16] Adachi S 2009 *Properties of semiconductor alloys* (West Sussex: Wiley)

[17] Lee B H 1970 *J. Appl. Phys.* **41** 2988

[18] Lehoczky A, Nelson D A and Whitsett C R 1969 *Phys. Rev.* **188** 1069

[19] Ford P J, Miller A J, Saunders G A, Yourtçu Y K, Furdyna J K and Jaczynski M 1982 *J. Phys. C: Sol. Stat. Phys.* **15** 657

[20] Berlincourt D, Jafee H and Shlozawa L R 1963 *Phys. Rev.* **129** 1009

[21] Cline C F, Dunegan H L and Henderson G W 1967 *J. Appl. Phys.* **38** 1944

[22] Phillips J C 1970 *Rev. Mod. Phys.* **42** 317

[23] Kumazaki K 1976 *Phys. Status Solidi A* **33** 615

[24] Strehlow W H and Cook E L 1973 *J. Phys. Chem. Ref. Data* **2** 163

[25] Einfeldt S, Goschenhofer F, Becker C R and Landwehr G 1995 *Phys. Rev. B* **51** 4915

[26] Manabe A, Mitsuishi A and Yoshinaga H 1967 *Jpn. J. Appl. Phys.* **6** 593

[27] Chen X J, Mintz A, Hu J S, Hua X L, Zinck J and Goddard W A I I I 1995 *J. Vac. Sci. Technol. B* **13** 1715

[28] Heyd J, Peralta J E and Scuseria G E 2005 *J. Chem. Phys.* **123** 174101

[29] Deligoz E, Colakoglu K and Ciftci Y 2006 *Physica B* **373** 124

[30] Ouendadji S, Ghemid S, Meradji H and El Haj Hassan F 2011 *Comp. Matr. Sci.* **50** 1460

[31] Guo L, Zhang S, Feng W, Hu G and Li W 2013 *J. Alloys Comp.* **579** 583

[32] Sharma S, Verma A S, Sarkar B K, Bhandari R and Jindal V K 2011 *AIP Conf. Proc.* **1393** 229

[33] Rabani E 2002 *J. Chem. Phys.* **116** 258

[34] Kamran S, Chen K and Chen L 2008 *Phys. Rev. B* **77** 094109

[35] Ullah N, Murtaza G, Khenata R, Wong K M and Alahmed Z A 2014 *Phase Transit.* **87** 571

[36] Al Shafaay B, El Haj Hassan F and Korek M 2014 *Comp. Mater. Sci.* **83** 107

[37] Duz I, Erdem I, Ozdemir Kart S and Kuzucu V 2016 *Arch. Mater. Sci. Eng.* **79** 5

[38] El Haj Hassan F, Al Shafaay B, Meradji H, Ghemid S, Belkhir H and Korek M 2011 *Phys. Scr.* **84** 065601

[39] Khenata R, Bouhemadou A, Sahnoun M, Reshak A H, Baltache H and Rabah M 2006 *Comp. Mater. Sci.* **38** 29

[40] Casali R A and Christensen N E 1998 *Sol. Stat. Commun.* **108** 793
[41] Bilal M, Shafiq M, Ahmad I and Khan I 2014 *J. Semicond.* **35** 0720011
[42] Varshney D, Shriya S and Khenata R 2012 *Mater. Chem. Phys.* **135** 365
[43] Fleszar A and Hankew, 2005 *Phys. Rev. B* **71** 045207
[44] Zakharov O, Rubio A, Blasé X, Cohen M L and Loui S G 1994 *Phys. Rev. B* **50** 10780
[45] Boutaiba F, Zaoui A and Ferhat M 2009 *Superlattices Microst.* **46** 823
[46] Benkert A, Schumacher C and Brunner K 2007 *Appl. Phys. Lett.* **90** 162105
[47] Tournie E, Ongaretto C, Laugt M and Faurie J P 1998 *Appl. Phys. Lett.* **72** 217
[48] Rafipoor M, Dupont D, Tornatzky H, Tessier M D, Maultzsch J, Tessier M D *et al* 2018 *Chem. Mater.* **30** 4393
[49] Yeh C-W, Chen G-H, Ho S-J and Chen H-S 2019 *Nano Mater.* https://doi.org/10.1021/acsanm.9b01213
[50] Sparing L M, Mintairov A M, Hodak J H, Martini I B, Hartland G V, Bindley U *et al* 2000 *J. Appl. Phys.* **87** 3063
[51] Wu J D, Huang Y S, Li B S, Shen A, Tamargo M C and Tiong K K 2010 *J. Appl. Phys.* **108** 123105
[52] Hara K, Machimura H, Usui M, Munekata H, Kukimoto H and Yoshino J 1995 *Appl. Phys. Lett.* **66** 3337
[53] Mycielski A, Kossutt J, Dobrowolskat M and Dobrowolskit W 1982 *J. Phys. C: Sol. Stat. Phys.* **15** 3293
[54] Sarkar P and Springborg M 2003 *Phys. Rev. B* **68** 235409
[55] Goswami B, Pal S, Sarkar P, Seifert G and Springborg M 2006 *Phys. Rev. B* **73** 2053124
[56] Goswami B, Pal S and Sarkar P 2007 *Phys. Rev. B* **76** 045323
[57] Saha S, Pal S, Sarkar P, Rosa A L and Frauenheim T 2012 *J. Comput. Chem.* **33** 1165
[58] Kaledin A L, Kong D, Wu K, Lian T and Musaev D G 2018 *J. Phys. Chem. C* **122** 18742
[59] Kar M, Sarkar R, Pal S and Sarkar P 2020 *Phys. Rev. B* **101** 195305
[60] Benchikh K, Abid H and Benchehima M 2017 *Mater. Sci. Pol.*, https://doi.org/10.1515/msp-2017-0005
[61] Debbarma M, Sarkar U, Debnath B, Ghosh D, Chanda S, Bhattacharjee R and Chattopadhyaya S 2018 *Curr. Appl. Phys.* **18** 698
[62] Murtaza G, Ullah N, Rauf A, Khenata R, Omran S B, Sajjad M *et al* 2015 *Mater. Sci. Semicond. Process.* **30** 462
[63] Debbarma M, Sarkar U, Debnath B, Ghosh D, Chanda S, Bhattacharjee R *et al* 2018 *J. Alloys Comp.* **748** 446
[64] Hohenberg P and Kohn W 1964 *Phys. Rev. B* **136** 864
[65] Kohn W and Sham L J 1965 *Phys. Rev.* **140** A1133
[66] Andersen O K 1975 *Phys. Rev. B* **42** 3063
[67] Blaha P, Schwarz K, Madsen G H, Kbasnicka D and Luitz J 2001 in Schwarz K (ed.) *FP-LAPW+lo program for calculating crystal properties, 2nd edn. Vienna University of Technology, Vienna*
[68] Togo A, Oba F and Tanaka I 2008 *Phys. Rev. B* **78** 134106
[69] Jamal M, Asadabadi S J, Ahmed I and Aliabad H A R 2014 *Comp. Mater. Sci.* **95** 592
[70] Perdew J P, Burke K and Ernzerhof M 1996 *Phys. Rev. Lett.* **77** 3865
[71] Tran F and Blaha P 2009 *Phys. Rev. Lett.* **102** 226401
[72] Anisimov V I, Zaanen J and Andersen O K 1991 *Phys. Rev. B* **44** 943
[73] Anisimov V I, Solovyev I V, Korotin M A, Czyyk M T and Sawatzky G A 1993 *Phys. Rev. B* **48** 16929
[74] Hubbard J 1963 *Proc. Roy. Soc. Lond. A* **276** 238
[75] Kokalj A 2003 *Comp. Mat. Sci.* **28** 155
[76] Murnaghan F D 1944 *Proc. Natl. Acad. Sci. USA* **30** 244
[77] Vegard L 1921 *Z. Phys.* **5** 17
[78] Pettifor D G 1992 *Mater. Sci. Technol.* **8** 345
[79] Li S, Li S and Ju X 2017 *J. Alloys Comp.* **695** 2916
[80] Potter R Y 1957 *J. Phys. Chem. Solids* **3** 223
[81] Huang W and Yang L 2015 *Can. J. Phys.* **93** 1
[82] Liu B, Wang J Y, Li F Z and Zhou Y C 2010 *Acta Mater.* **58** 4369
[83] Fine M E, Brown L D and Marcus H L 1984 *Scr. Metall.* **18** 951
[84] Fox M 2001 *Optical properties of solids* (UK: Oxford University Press)
[85] Penn D R 1962 *Phys. Rev.* **128** 2093